CHAPTER

1

Bioheat Transfer and Thermal Heating for Tumor Treatment

Huang-Wen Huang[a], *Tzyy-Leng Horng*[b]

[a]Tamkang University, Taipei, Taiwan

[b]Feng Chia University, Taichung, Taiwan

OUTLINE

1.1 PENNES' AND OTHER BIOHEAT TRANSFER EQUATIONS

1.1.1 Introduction

The investigation of heat transfer and fluid flow in biological processes requires accurate mathematical models. Biological processes basically involve two phases—solid and liquid (fluid). During the past 50 years, through development of thermal modeling in biological processes, heat transfer processes have been established that include the impact of fluid flow which is due to blood. Table 1.1 shows the significance of thermal transport modes in typical components of biothermal systems, as our subject of discussion refers to cancer treatments using heat. For example, thermal diffusion plays a dominant transport mode in tissues, and convection is less significant as blood perfuses in solid tissues at capillary level vessels (which are small in size and slow in blood motion).

TABLE 1.1 Significance of Thermal Transport Modes in Typical Components of Biothermal Systems

	Conduction	Convection	Radiation
Tissues	Significant	Less significant	Insignificant
Bones	Significant	Insignificant	Insignificant
Blood vessels	Less significant	Significant	Insignificant
Skins	Insignificant	Significant	Significant

TABLE 1.2 Temperature Ranges with Their Tissue Interactions in Biological Processes

Temperature range (°C)	Interaction and terminology with tissues
35-40	Normothermia
42-46	Hyperthermia
46-48	Irreversible cellular damage at 45 min
50-52	Coagulation necrosis, 4-6 min
60-100	Near instantaneous coagulation necrosis
> 110	Tissue vaporization

Thermal ablation therapy is an application of heat transfer and fluid flow in biological processes. Temperature plays a significant role with tissue interactions (e.g., coagulation necrosis). To give readers a picture of temperature treatments with tissue (and terminology), Table 1.2 shows temperature ranges with their tissue interactions in biological processes. A thermal model that satisfied the following three criteria was needed to predict temperatures in a perfused tissue: (1) the model satisfied conservation of energy; (2) the heat transfer rate from blood vessels to tissue was modeled without following a vessel path; and (3) the model applied to any unheated and heated tissue. To meet these criteria, many research groups around the world have proposed mathematical models in an attempt to properly describe the heat transfer and fluid flow in biological processes in a heated, vascularized, finite tissue by making a few simplifying assumptions. We will highlight some of the key models and some models considering the impact of large blood vessel(s) by starting with Pennes' model.

1.1.2 Pennes' Bioheat Transfer Equation

The Pennes' [1] bioheat transfer equation (PBHTE) has been a standard model for predicting temperature distributions in living tissues for more than a half century. The equation was established by conducting a sequence of experiments measuring temperatures of tissue and arterial blood in the resting human forearm. The equation includes a special term that describes the heat exchange between blood flow and solid tissues. The blood temperature is assumed to be constant arterial blood temperature.

In 1948, Pennes [1] performed a series of experiments that measured temperatures on human forearms of volunteers and derived a thermal energy conservation equation: the well-known bioheat transfer equation (BHTE) or the traditional BHTE. Tissue matrix thermal equations can be explained most succinctly by considering the PBHTE as the most general formulation. It is written as:

$$\nabla \cdot k \nabla T + q_{\mathrm{p}} + q_{\mathrm{m}} - W c_{\mathrm{b}} (T - T_{\mathrm{a}}) = \rho c_{\mathrm{p}} \frac{\partial T}{\partial t}, \tag{1.1}$$

where $T(^{\circ}\mathrm{C})$ is the local tissue temperature, $T_{\mathrm{a}}(^{\circ}\mathrm{C})$ is the arterial temperature, $c_{\mathrm{b}}(\mathrm{J/kg/^{\circ}C})$ is the blood specific heat, $c_{\mathrm{p}}(\mathrm{J/kg/^{\circ}C})$ is the tissue specific heat, $W(\mathrm{kg/m^3/s})$ is the local tissue-blood perfusion rate, $k(\mathrm{w/m/^{\circ}C})$ is the tissue thermal conductivity, $\rho(\mathrm{kg/m^3})$ is the tissue density, $q_{\mathrm{p}}(\mathrm{w/m^3})$ is the energy deposition rate, and $q_{\mathrm{m}}(\mathrm{w/m^3})$ is the metabolism, which is usually very small compared to the external power deposition term q_{p} [2]. The term $W c_{\mathrm{b}}(T - T_{\mathrm{a}})$, which accounts for the effects of blood perfusion, can be the dominant form of energy removal when considering heating processes. It assumes that the blood enters the control volume at some arterial temperature T_{a}, and then comes to equilibrium at the tissue temperature. Thus, as the blood leaves the control volume it carries away the energy, and hence acts as an energy sink in hyperthermia treatment.

Because Pennes' equation is an approximation equation and does not have a physically consistent theoretical basis, it is surprising that this simple mathematical formulation predicted temperature fields well in many applications. The reasons why PBHTE has been widely used in the hyperthermia modeling field are twofold: (1) its mathematical simplicity; and (2) its ability to predict the temperature field reasonably well in application.

Nevertheless, the equation does have some limitations. It does not, nor was it ever intended to, handle several physical effects. The most significant problem is that it does not consider the effect of the directionality of blood flow, and hence does not describe any convective heat transfer mechanism.

1.1.3 The Chen and Holmes Model

Several investigators have developed alternative formulations to predict temperatures in living tissues. In 1980, Chen and Holmes (CH) [3] derived one with a very strong physical and physiological basis. The equation can be written as:

$$\nabla \cdot \left(k + k_{\mathrm{p}}\right) \nabla T + q_{\mathrm{p}} + q_{\mathrm{m}} - W c_{\mathrm{b}} (T - T_{\mathrm{a}}) - \rho_{\mathrm{b}} c_{\mathrm{b}} u \cdot \nabla T = \rho c_{\mathrm{p}} \frac{\partial T}{\partial t}. \tag{1.2}$$

Comparing this equation with Pennes' equation, two extra terms have been added. The term $-\rho_{\mathrm{b}} c_{\mathrm{b}} u \cdot \nabla T$ is the convective heat transfer term, which accounts for the thermal interactions between blood vessels and tissues. The term $\nabla \cdot k_{\mathrm{p}} \nabla T$ accounts for the enhanced tissue conductive heat transfer due to blood perfusion term in tissues, where k_{p} is called the perfusion conductivity, and is a function of the blood perfusion rate. The blood perfusion term $-W c_{\mathrm{b}}(T - T_{\mathrm{a}})$, shown in the CH model, accounts for the effects of the large number of capillary structures whose individual dimensions are small relative to the macroscopic phenomenon under their study. Relatively, the CH model has a more solid physical basis than Pennes' model. However, it requires knowledge of the details of the vascular anatomy and flow

pattern to solve it, and while this does increase the accuracy, it adds a great deal of complication to the solution.

1.1.4 The Weinbaum and Jiji Model

In 1985, Weinbaum and Jiji (WJ) [4] proposed an alternative mathematical formulation of the BHTE. Their formulation is based on their observations from the vascular network of rabbit thighs that blood vessels that are significant for heat transfer in tissues always occur in countercurrent pairs. Hence, the major heat transfer mechanism between blood and tissues is the "incomplete countercurrent heat exchanger" between thermally significant arteries and veins (with diameters about 50-500 μm). Their formulation uses tensor notation and it can be written as:

$$\rho c\frac{\partial\theta}{\partial t}-\frac{\partial}{\partial x_i}\left[\left(k_{ij}\right)_{\text{eff}}\frac{\partial\theta}{\partial x_j}\right]=-\frac{\pi^2 na^2k_{\text{b}}^2}{4\sigma k}Pe^2l_j\frac{\partial l_i}{\partial k_j}\frac{\partial\theta}{\partial x_j}+Q_{\text{m}}, \tag{1.3}$$

where θ is the local temperature, ρc is the volume average tissue density and specific heat product, a is the local blood vessel radius, σ is a shape factor for the thermal conduction resistance between adjacent countercurrent vessels, n is the number density of blood vessels of size a, k_{b} is the blood thermal conductivity, Pe is the local Peclet number (=2 ρ_{b}cnau$/k_{\text{b}}$), u is average blood flow velocity in the vessels, and l_i is the direction cosine of the ith pair of countercurrent vessels (i.e., ϕ is the angle of the ith pair of countercurrent vessels' axes relative to the temperature gradient and l_i is expressed as cos ϕ). The effective conductivity tensor element, $(k_{ij})_{\text{eff}}$, is given by:

$$\left(k_{ij}\right)_{\text{eff}}=k\left(\delta_{ij}+\frac{\pi^2 na^2k_{\text{b}}^2}{4\sigma k^2}Pe^2l_il_j\right), \tag{1.4}$$

where δ_{ij} is the kronecker delta function, and k is the tissue thermal conductivity. Clearly, this equation represents one of the most significant contributions to the bioheat transfer formulation. However, in practical situations, this equation needs detailed knowledge of the sizes, orientations, and blood flow velocities in the countercurrent vessels to solve it and that presents a formidable task. Furthermore, there are several issues related to the WJ model. First, thorough comparisons for both predicted temperatures and macroscopic experiments are required. Second, the formulation was developed for superficial normal tissues in which countercurrent heat transfer occurs. In tumors, the vascular anatomy is different from the superficial normal tissues, and therefore a new model should be derived for tumors. Wissler [5,6] has questioned the two basic assumptions of the WJ model: first, that the arithmetic mean of the arteriole and venule blood temperature can be approximated by the mean tissue temperature; and second, that there is negligible heat transfer between the thermally significant arteriole-venule pairs and surrounding tissue.

1.1.5 The Weinbaum, Jiji, and Lemons Model

The Weinbaum, Jiji, and Lemons (WJL) model [7] attempted to describe the blood flow effect in the heat transfer process when limited to small blood vessels. Keller and Seiler [8] used the effective conductivity of the nonisothermal region, which is determined under various blood flow conditions. The WJL model's approach resembles that of Keller and Seiler [8]

mathematically in its use of three equations, but the WJL model is based on completely different vascular generations—the WJL equations apply to thermally significant small vessels and not to major supply blood vessels.

1.1.6 Baish et al

According to Baish et al. [9,10], one of the underlying assumptions in deriving the WJ model was that, due to the proximity of the vessels in a countercurrent pair, almost all of the heat conducted through the arterial wall reaches the venous wall—a process in which the temperature of the tissue between the vessels remains unaffected. They [9,10] criticized this hypothesis, postulating that part of the heat leaving the wall of a small arteriole will remain within the tissue. They suggested that the heat transfer between countercurrent vessels depends not only on $T_a - T_v$, but also on the difference between the tissue temperature, T, and the average blood temperature, $(T_a + T_v)/2$. T_a is the arterial temperature and T_v is the venous temperature.

1.1.7 Others

Efforts have been directed, for the most part, toward the WJL and WJ models. Following the publication of the CH, WJL, and WJ models, several studies were performed to evaluate the validity of these new approaches. Here are some arguments and approximations to examine the blood flow impacts on biothermal modeling.

In 1987, Wissler [5,6] strongly criticized the WJ model because of the assumption made on the blood temperature at arterial and venous vessels as well as the nearby tissue temperature. Wissler proposed a new model that described tissue-blood vessels heat exchange that differs from the respective equations in WJL by virtue of an additional perfusion term. For example, temperature profiles along an artery-vein pair is approximated as $T \approx \frac{(T_a + T_v)}{2}$ in the WJ model. He rejected the hypothesis that blood and tissue temperatures are closely coupled which was basically used for the derivation of the thermal conductivity tensor defined in the WJL equation. The thermal conductivity tensor form in the WJL equation is to remove the blood flow term.

During 1989-1990, Charny et al. [11,12] introduced a "modified" WJL model for the blood vessels by changing the governing equation with a tissue energy conservation equation. Based on their analysis of both steady state and transient temperature fields in the limb under hyperthermic and normothermic conditions, the tissue temperature profiles predicted by that model were very similar to those predicted by Pennes' model in the tissue regions with large vessels ($d > 0.4$ mm).

1.2 BLOOD FLOW IMPACTS ON THERMAL LESIONS WITH PULSATION AND DIFFERENT VELOCITY PROFILES

In this section, we will develop a solution to PBHTE coupled with an energy transport equation of pulsatile blood flow in a thermally significant blood vessel surrounded by a tumor tissue. The purpose of this design is to study the cooling effect of pulsatile blood flow in large blood vessels.

1.2.1 Introduction

Though PBHTE, shown in Equation (1.1), is the most popular model in hyperthermia modeling, a fundamental criticism of this model by Nelson [13] is that the treatment of blood flow term as a distributed heat source (or sink) mistakenly presumes that the capillary vasculature is the major site of heat exchange. In other words, the blood flow term is a scalar property. In fact, the blood flow in a tissue usually has a direction from artery to vein passing through the capillary bed. Furthermore, the blood and its surrounding tissues are not in thermal equilibrium when the blood vessel diameter is larger than 500 μm [14–22]. This means the energy equations for tissue and blood in significantly large vessels must be treated individually.

One of the key issues of thermal treatments is blood flow. Blood flow usually drains the delivered heat from the heating region, which causes insufficient thermal dose in the targeted volume. This is an important factor needing to be considered carefully in thermal treatments [23–26]. In fact, the differential therapeutic effect of thermal treatments between malignant and normal tissue may primarily depend on the vascular characteristics of the tumor [27]. Craciunescu and Clegg [28] solved the fully coupled Navier-Stokes and energy equations to obtain the temperature distribution of pulsatile blood flow within a rigid blood vessel. They found that the reversed flow enhances as the Womersley number becomes larger, which results in a smaller temperature difference between forward and reverse flows. Nevertheless, in their model they only focused on the temperature distribution in blood vessels without considering the surrounding tissue. Khanafer et al. [26] and Horng et al. [29] further studied the effects of pulsatile blood flow on temperature distributions during hyperthermia by considering both the pulsatile blood flow in a blood vessel and its surrounding tissue. Here we focus on the results of Horng et al. [29] to discuss how the blood flow velocity profile (including pulsation frequency), size of blood vessel (including blood flow rate), and heating rate affect the thermal dose distribution of the surrounding tissue during heat treatment.

1.2.2 Mathematical Model and Numerical Method

1.2.2.1 Velocity Profile of Pulsatile Blood Flow in a Circular Blood Vessel

It is of interest to not only consider simple steady uniform or parabolic blood velocity profile, but also the pulsatile blood flow in thermally significant blood vessels (i.e., larger than 200 μm in diameter) [23,25,29], with the assumptions that the blood vessel segment is straight, the vessel wall is rigid and impermeable, and the flow is incompressible and Newtonian. Considering the steady blood flow passing through a rigid vessel of inner radius r_0, the axial Hagen-Poiseuille velocity profile can be expressed as:

$$w(r) = -\frac{1}{4\mu}\left(r_0^2 - r^2\right)\frac{\mathrm{d}p}{\mathrm{d}z}, \tag{1.5}$$

where μ is the dynamic viscosity and $\frac{\mathrm{d}p}{\mathrm{d}z}$ the constant pressure gradient along the axial (z) direction. Because the blood flow in the cardiovascular system is periodic, the pressure gradient cannot remain a constant. Here, it is modified to have an additional sinusoidal component in time, shown as follows:

$$\frac{\partial p}{\partial z} = c_0 + c_1 \mathrm{e}^{\mathrm{i}\omega t},$$

where ω is the angular frequency and the associated period of time is denoted as $\widetilde{T} = \frac{2\pi}{\omega}$. Then the corresponding axial velocity profile, $W(r,t)$, can be expressed as:

$$W(r,t) = w(r) + w_1(r)e^{i\omega t}. \tag{1.6}$$

Here, c_0 can be related to the average volume flow rate over the time period $\widetilde{T}$ as follows:

$$\dot{Q}_{\text{avg}} = \frac{1}{\widetilde{T}}\int_0^{\widetilde{T}}\int_0^{r_0} 2\pi W r dr dt = -\frac{\pi r_0^4}{8\mu}c_0. \tag{1.7}$$

The average velocity can be further deduced from above:

$$\overline{w} = \frac{\dot{Q}_{\text{avg}}}{\pi r_0^2} = -\frac{c_0 r_0^2}{8\mu}, \tag{1.8}$$

and $w(r)$ can then be alternatively expressed as:

$$w(r) = 2\overline{w}\left(1 - \frac{r^2}{r_0^2}\right). \tag{1.9}$$

The term w_1 can be derived from the Navier-Stokes equations [30]. Together with $w(r)$ in Equation (1.9), $W(r,t)$ in Equation (1.6) can be expressed as follows:

$$W(r,t) = 2\overline{w}\left(1 - \frac{r^2}{r_0^2}\right) + \frac{ic_1 r_0^2}{\mu\alpha^2}\left[1 - \frac{J_0\left(\alpha\frac{r}{r_0}i^{\frac{3}{2}}\right)}{J_0\left(\alpha i^{\frac{3}{2}}\right)}\right]e^{i\omega t}, \tag{1.10}$$

where $\alpha = \frac{r_0}{\sqrt{\nu/\omega}}$ denotes the Womersley number describing the competition between the inertia and viscous forces; ν denotes the kinematic viscosity of blood; and J_0 is the Bessel function of the first kind of order zero. If oscillatory driving pressure gradient is $c_1\cos(\omega t)$, the corresponding velocity will then be the real part of Equation (1.10). If the oscillatory driving pressure gradient is $c_1\sin(\omega t)$, the corresponding velocity will then be the imaginary part of Equation (1.10). Here we also define

$$\text{fac} = c_1/c_0 = c_1\Big/\left(-\frac{8\mu\overline{w}}{r_0^2}\right), \tag{1.11}$$

and use it to characterize the relative intensity of pulsation in the blood flow. Reasonable value of fac ranging from 0.2 to 1 is considered here. When the Womersley number, α, is large, the effect of viscosity cannot propagate far from the vessel wall, and the blood flow in the central part of a vessel acts like an inviscid flow and can be chiefly determined by the balance between the inertia force and the pressure gradient. Under this situation, the velocity profile of an oscillatory component has a rather flattop shape at certain phases compared with a parabolic profile of Poiseuille flow. When the Womersley number, α, is large enough, the velocity profile of an oscillatory component may even display two peaks at certain phases [29,31]. Some examples of the diameters of thermally significant blood vessels and their associated average velocities are listed in Table 1.3 [29]. Taking the largest blood vessel considered in

TABLE 1.3 List of the Blood Vessel Parameters Used in Current Study

Diameter (mm)	Average blood velocity in tumor ($\overline{w}$) (mm/s)
0.2	3.4
0.6	6
1.0	8
1.4	10.5
2.0	20

Table 1.3 (diameter = 2 mm), and varying heart beat frequency from 1 to 3 Hz as suggested by Huo and Kasab [32], the velocity profiles of an oscillatory component are respectively shown in Figure 1.1 at selected time phases. It can be observed that, as the Womersley number increases with increasing beating frequency, the oscillatory velocity component exhibits flat-top and even two-peak behaviors.

1.2.2.2 *Governing Equations and Numerical Method*

Here we assume that the absorbed power density in blood and tissue is equal to the heating power density. Although this is a very limiting assumption and generally not true, it still serves its purpose because we focus our study on the cooling effect of large blood vessels here. The axis-symmetric geometric configuration considered here is a cylindrical perfused tissue, including tumor and normal tissues, with a coaxial rigid blood vessel inside and throughout the tissue as shown in Figure 1.2. The whole computational domain is bounded by $r = r_{max}$, $z = 0$, and $z = z_{max}$; the blood vessel is surrounded by $r = r_0, z = 0$, and $z = z_{max}$; and the heating target (tumor and a part of blood vessel inside the tumor) is bounded by $r = r_1, z = z_1$, and $z = z_2$. The diameters of blood vessels and their associated average flow velocities considered in the study of this section are presented in Table 1.3.

Under the axis-symmetric geometric configuration mentioned above, the governing equations for the temperature evolution are PBHTE in Equation (1.12) for tissue and energy transport equation in Equation (1.13) for blood vessels:

$$\rho_t c_t \frac{\partial T_t}{\partial t} = k_t \left[\frac{1}{r} \frac{\partial}{\partial r} \left(r \frac{\partial T_t}{\partial r} \right) + \frac{\partial^2 T_t}{\partial z^2} \right] - W_b c_b (T_t - T_a) + Q_t(r, z, t), \tag{1.12}$$

$$\rho_b c_b \left(\frac{\partial T_b}{\partial t} + w \frac{\partial T_b}{\partial z} \right) = k_b \left[\frac{1}{r} \frac{\partial}{\partial r} \left(r \frac{\partial T_b}{\partial r} \right) + \frac{\partial^2 T_b}{\partial z^2} \right] + Q_b(r, z, t), \tag{1.13}$$

where $T(r, z, t)$ denotes the temperature that is distributed axis-symmetrically; ρ, k, c are density, thermal conductivity, and specific heat, respectively, that are all assumed to be constant; $Q(r, z, t)$ is the power of heat added axis-symmetrically; W_b is the perfusion mass flow rate; T_a is the ambient temperature that is usually set to be 37 °C; $w(r, t)$ is that axial velocity of blood flow; and subscripts t and b represent tissue and blood, respectively. Notice that in the study of this section the tissue metabolic heat production Q_m is neglected compared with heating power as mentioned in Section 1.1.2. The heat sink $-W_b c_b (T_t - T_a)$ in Equation (1.12) is used to describe the perfusion effect by the microvascular network of blood flow (i.e., blood vessels with diameter generally less than 200 μm), while the heat transfer due to the thermally significant large

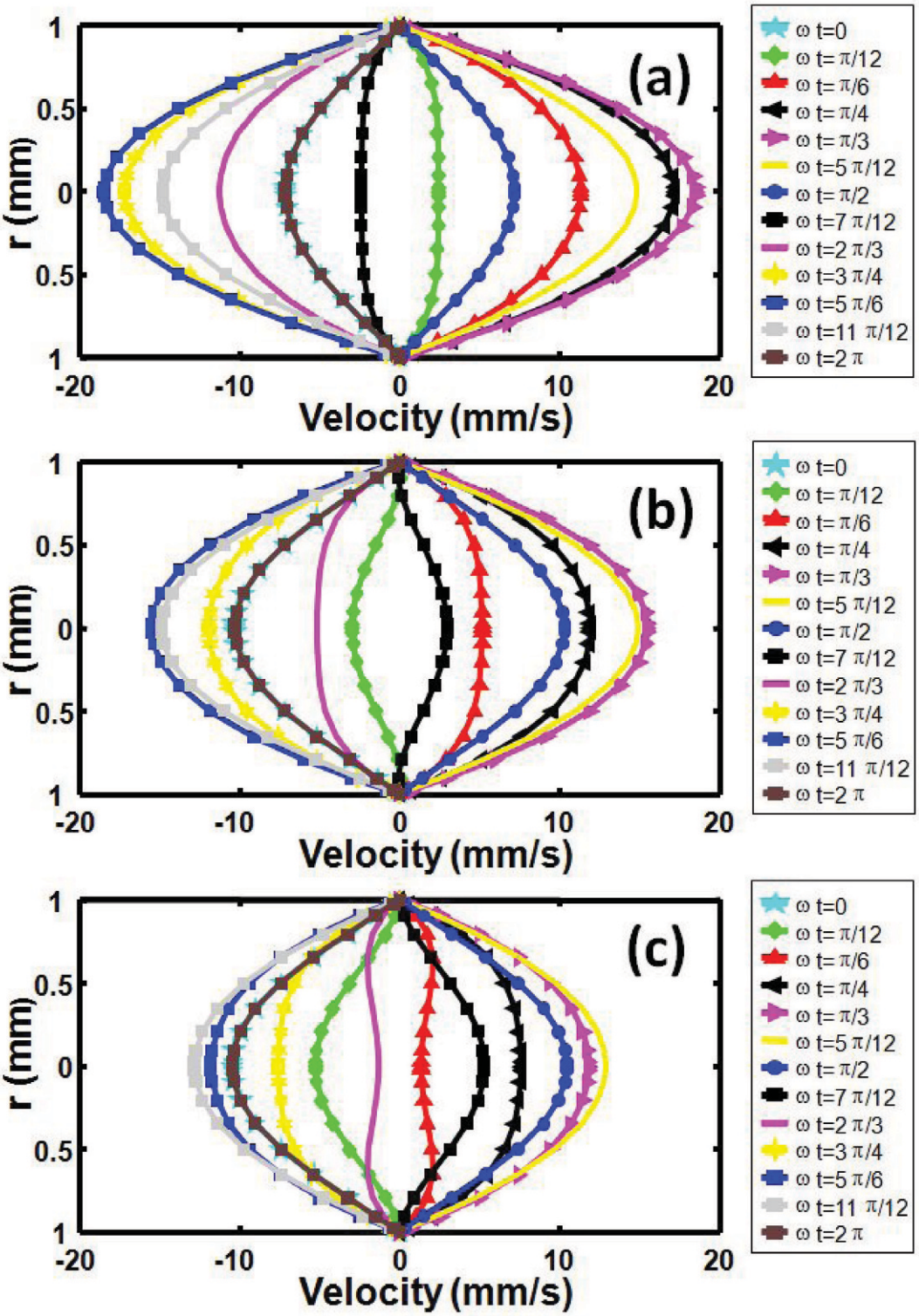

FIGURE 1.1 Effect of Womersley number, α, on the oscillatory component of the velocity profile for blood flow with blood vessel diameter being 2 mm. The velocity profile is shown at several selected phases between 0 and 2π for (a) $f=1$ Hz, $\alpha=1.2843$, (b) $f=2$ Hz, $\alpha=1.8162$, and (c) $f=3$ Hz, $\alpha=2.2244$. Flattop and two peak features can be observed when α is large as shown in (c). The Womersley number is calculated based on the density of blood $\rho_b=1050$ kg/m^3, and dynamic viscosity of blood $\mu_b=4\times10^{-3}$ Pas.

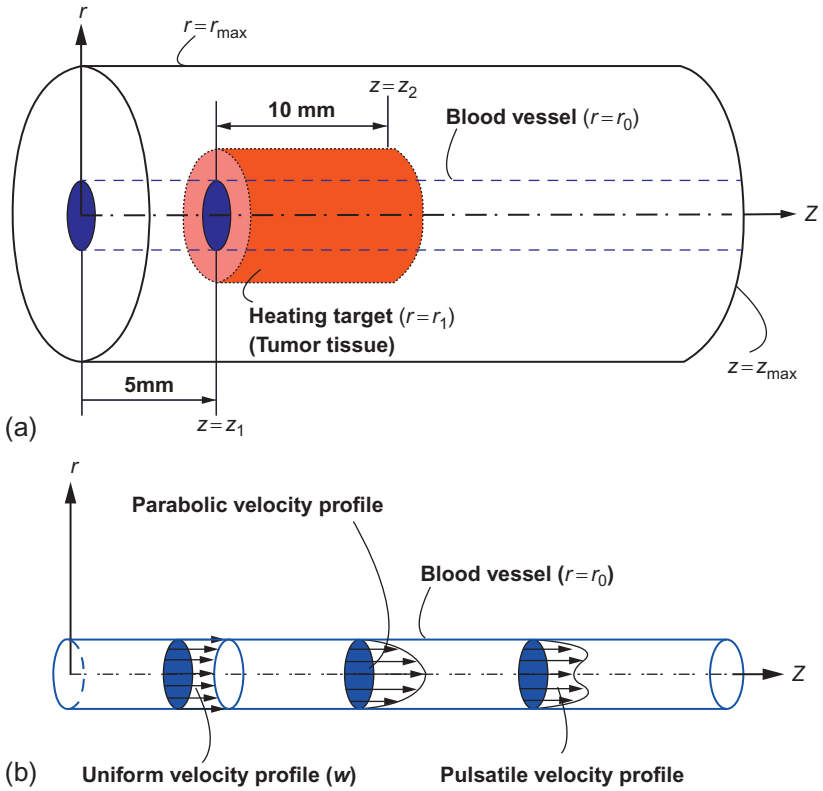

FIGURE 1.2 Geometric configuration in current simulations. (a) The treatment target (heating target) is specified as $z_1 \le z \le z_2, 0 \le r \le r_1$, with $z_1 = 5$ mm, $z_2 = 15$ mm, $r_1 = 5$ mm considered here. (b) Schematic illustration of the three kinds of velocity profile of blood flow in blood vessels. Left: steady uniform velocity profile; Middle: steady parabolic velocity profile; Right: pulsatile velocity profile.

blood vessel has to be separately described by Equation (1.13). Together with initial, boundary, and interface conditions (see details in Ref. [29]), Equations (1.12) and (1.13) were numerically solved by the highly accurate multiblock Chebyshev pseudospectral method under the framework of method of lines (MOL). Notice that the computational domain is decomposed to nine blocks and is shown in Figure 1.3 with numerical meshes. Blocks 1, 2, and 3 are the blood vessel; block 5 is the tumor; the others are normal tissue. Heating zones are blocks 2 and 5. For further numerical details, see Horng et al. [29] and Shih et al. [33].

1.2.2.3 *Calculation of Thermal Dose*

The accumulated thermal dose to tissue is a function of heating duration and the temperature level. The estimate of tissue damage is based on the thermal dose the formula for which was proposed by Sapareto and Dewey [34]. The thermal dose or equivalent minutes at 43 °C (EM_{43}) is shown as follows:

$$EM_{43}(\text{in min}) = \int_0^{t_f} R^{T-43} dt, \tag{1.14}$$

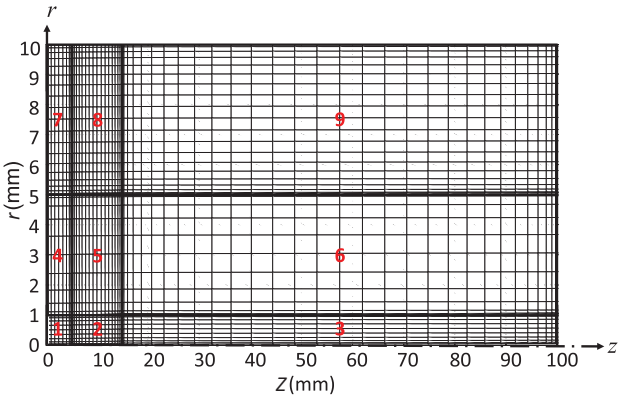

FIGURE 1.3 The overall computational domain is decomposed into nine rectangular blocks in $r-z$ coordinates. Notice that blocks 1-3 are for the blood vessel, and blocks 4-9 are for the tissue with block 5 being the tumor and the others being the normal tissue. Heating zone indicated in Figure 1.2(a) would be blocks 2 and 5.

TABLE 1.4 Parameters of Six Different Heating Schemes Used in Current Study

Heating case	I	II	III	IV	V	VI
Heating power density Q (W/cm^3)	100	50	25	10	5	2
Heating duration t_h (s)	1	2	4	10	20	50
Total heated energy density (J/cm^3)	100	100	100	100	100	100

where $R=2$ for $T\geq 43$ °C, $R=4$ for 37 °C $<T<43$ °C, and $t_f=60$ s in the study of this section. The threshold dose for necrosis is $EM_{43}=240$ min for tumor muscle tissue, and the region encircled by the level curve $EM_{43}=240$ min is taken as the thermal lesion region. Covering tumor tissue but not normal tissue by thermal lesion region as fully as possible is most desired in the thermal treatment, though normal tissue may still survive at such a thermal dose because of the fact that tumor tissue is much less heat-bearable than normal tissue. If we define the deficit region as the tumor region excluding a thermal lesion region, it would serve as an evaluation of the effectiveness of the treatment. This region is greatly influenced by the size of the blood vessel [34] and the heating rate [35]. Six different heating schemes characterizing different heating rates under the same amount of heat added (100 J/cm^3 from preliminary energy analysis in lump [36]) are depicted in Table 1.4.

1.2.3 Results and Discussions

Figure 1.4 compares the effects of steady uniform and parabolic velocity profiles for blood flow on a thermal lesion region with heating scheme II in Table 1.4. Likewise, Figure 1.5 compares the effects of pulsatile blood flow with various pulsatile frequencies (1, 1.5, and 2 Hz) with the relative intensity of pulsation fac = 0.2 on a thermal lesion region with the same heating scheme. Figures 1.4 and 1.5 generally show that there is almost no difference in a thermal lesion region among all these velocity profiles under the same size of blood vessel. Only a

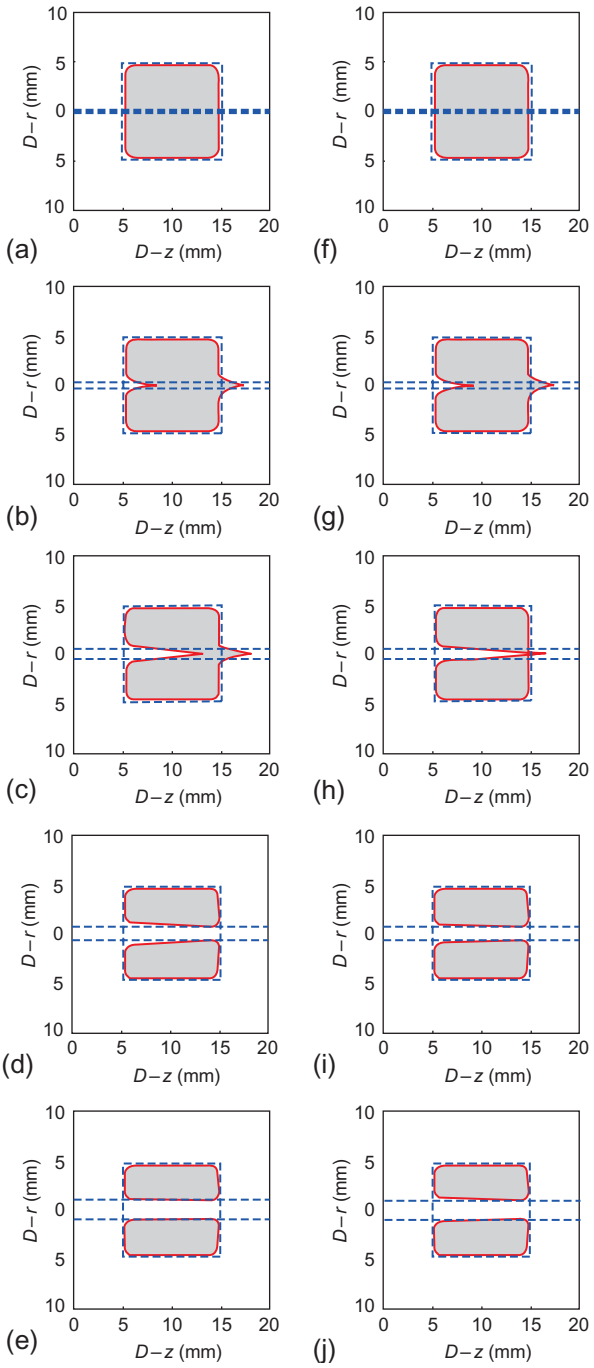

FIGURE 1.4 Effect of the steady velocity profiles of blood flow on the thermal lesion region (shaded region) for the blood vessels (a and f) 0.2 mm, (b and g) 0.6 mm, (c and h) 1 mm, (d and i) 1.4 mm, (e and j) 2 mm in diameter. (a-e) are results of a uniform velocity profile, and (f-j) are results of a parabolic one. The blood vessel boundaries are denoted with the horizontal dashed lines. The heated target region (tumor) is denoted by a square with dashed lines. Here $r_1 = 5$ mm, $W_b = 2\ \mathrm{kg/m^3/s^1}$, $\rho_b = \rho_t = 1050\ \mathrm{kg/m^3}$, $c_b = c_t = 3770\ \mathrm{J/kg^1/^\circ C^1}$, $k_b = k_t = 0.5\ \mathrm{W/m^3/^\circ C^1}$. The target is heated in the way of heating case II (i.e., $Q_t = Q_b = 50\ \mathrm{W/cm^3}$, and the heating duration = 2 s) in Table 1.4.

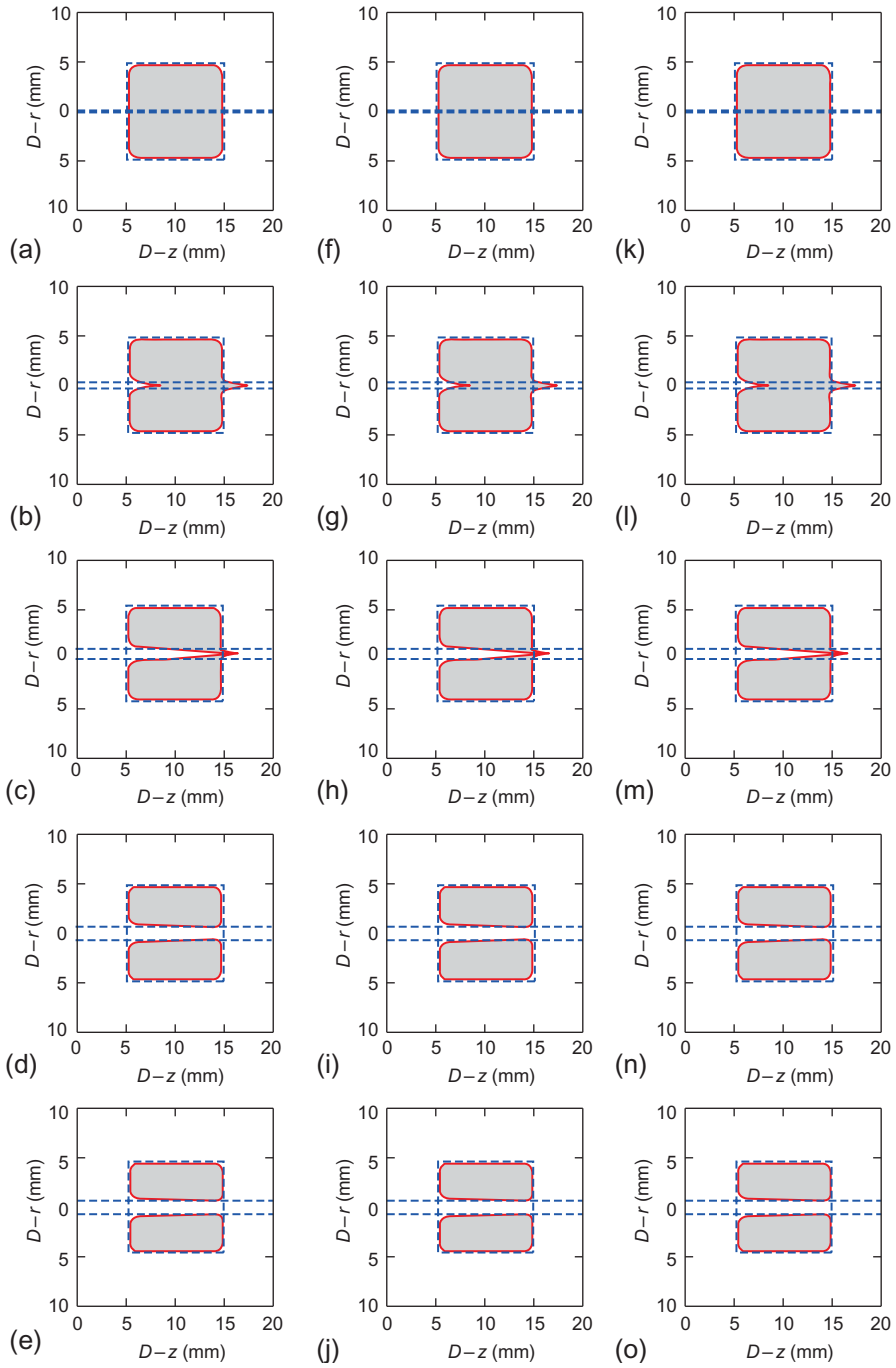

FIGURE 1.5 Effect of the frequency of the pulsatile blood flow on the thermal lesion region (shaded region) for the blood vessels (a, f, and k) 0.2 mm, (b, g, and l) 0.6 mm, (c, h, and m) 1 mm, (d, i, and n) 1.4 mm, (e, j, and o) 2 mm in diameter. (a-e) have the frequency 1 Hz, (f-j) have the frequency 1.5 Hz, and (k-o) have the frequency 2 Hz. The blood vessel boundaries are denoted with the horizontal dashed lines. The rest of the parameters and conditions are the same as Figure 1.4.

minor difference of the thermal lesion region in the blood vessel is observed in the middle-sized blood vessels (see details in Figure 1.6 of Horng et al. [29]).

Although the thermal lesion region is rather insensitive to the velocity profile of blood flow, it is deeply influenced by the size of the blood vessel because the heat convection by the blood flow in a blood vessel usually serves as a stronger heat sink than the blood perfusion in tissue. That means the temperature would drop faster in a blood vessel than in its surrounding tissue. This may cause a deficit in the thermal lesion region in the blood vessel and the surrounding tissue, which can be easily observed from Figures 1.4 and 1.5. Generally, the deficit of the thermal lesion region is less for smaller vessels. In the case of the smallest vessel (here with a diameter 0.2 mm), the thermal lesion region covers almost the entire blood vessel that is inside the tumor and the deficit is naturally the least. For the middle-sized vessels (here with diameters of 0.6 and 1 mm), the thermal lesion region in the blood vessel becomes smaller and shifts downstream. For large vessels (here with diameters of 1.4 and 2 mm), there is a total deficit of the thermal lesion region in the blood vessel, and this would cause a deficit in the tumor tissue near the blood vessel and especially in the upstream area.

Besides having a dependence on the blood vessel size, the thermal lesion region is also very sensitive to the heating rate. Figure 1.6 generally shows a larger thermal lesion region for

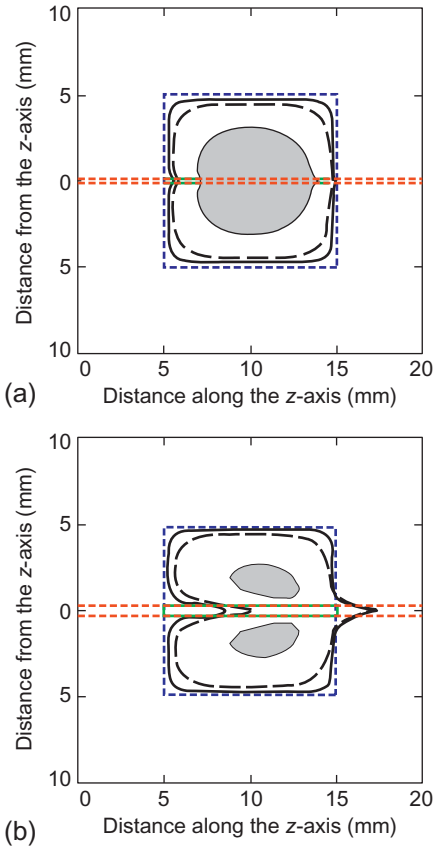

FIGURE 1.6 Comparison of the effect of different heating schemes and blood vessel diameters on the thermal lesion region with a steady uniform velocity profile. The solid and dashed lines represent heating cases II and IV, and the shaded area represents the heating case VI in Table 1.4. (a) The diameter of the blood vessel is 0.2 mm. (b) The diameter of the blood vessel is 1 mm.

faster heating, and there is a more pronounced effect on the heating rate when the blood vessel is larger. As shown in Figure 1.6b, there exists an obvious shift of thermal lesion region to the downstream of the blood vessel with diameter 1 mm when heating is fast, and this may cause unwanted thermal injury in normal tissue nearby. The effect of pulsation amplitude, in terms of relative intensity fac, of pulsatile blood flow on the thermal lesion region generally has little difference among various facs, except a minor difference for middle-sized blood vessels. This is further noted in Horng et al. [29] in the discussions of Figures 1.9–1.11. Generally, when fac increases, the blood flows more in a stick-slip fashion, and this may considerably influence the heat convection when incorporated with pulsation frequency. With large pulsation amplitudes like fac = 0.8 and 1, it even shows two-peak behavior in a thermal dose contour at the downstream of the blood vessel.

1.2.4 Conclusion

The current investigation shows that the effect of velocity profiles of blood flow, ranging from uniform, to parabolic, to pusatile, has almost no difference in the thermal lesion region on the tumor region and only a minor difference on the blood vessel when the blood vessel is of middle size. This result suggests that we might just as well use the simplest steady uniform or parabolic velocity profile to do the simulation. In fact, the thermal lesion region is much more sensitive to the heating rate and the size of the blood vessel. Faster heating would form a much better thermal lesion region, and it works best on small blood vessels with a better covering of both the tumor and the blood vessel by the thermal lesion region because the heat convection by the blood flow is least in the blood vessel. For large vessels, it has a total deficit in the blood vessel and some deficit in the tumor near the upstream of blood vessel. As to middle-sized vessels, a shift of a partially deficient thermal lesion region to the downstream of the blood vessel may cause unwanted thermal injury to the normal tissue nearby.

1.3 THERMAL RELAXATION TIME FACTOR IN BLOOD FLOW DURING THERMAL THERAPY

Non-Fourier heat conduction has been observed in biotissues, which implies PBHTE has to be modified by considering the thermal relaxation time factor. Here we study this effect under the same geometric configuration for tissue and blood vessel as in Section 1.2 to see how it affects hyperthermia generally.

1.3.1 Introduction

PBHTE, shown in Equation (1.1), is based on the classical Fourier law, which assumes that a temperature disturbance in any part of the materials leads to an instantaneous perturbation at each point of the whole. This implies that the propagation speed of thermal perturbation is infinite even when the intervening distance is very large, and causes some doubts and discussions [37–39]. Actually, non-Fourier heat conduction behavior has been observed in biomaterials with inhomogeneous inner structures [40], in biological tissues [41,42], in canine

thigh muscles [43], and in processed meats [44,45]. Considering the finite propagation speed for the thermal disturbance, Cattaneo [46] and Vernotte [47] formulated a modified heat flux equation, as shown in Equation (1.16) with the Fourier law shown in Equation (1.15) for comparison

$$q\left(\vec{r},t\right) = -k\nabla T\left(\vec{r},t\right), \tag{1.15}$$

$$q\left(\vec{r},t\right) + \tau\frac{\partial q\left(\vec{r},t\right)}{\partial t} = -k\nabla T\left(\vec{r},t\right), \tag{1.16}$$

where $T, q, k,$ and τ are temperature, heat flux, thermal conductivity, and thermal relaxation time, respectively. If we formally treat $-k\nabla T$ in Equation (1.16) as a constant A, the solution of Equation (1.16) would be simply:

$$q = A + B\mathrm{e}^{-\frac{t}{\tau}}. \tag{1.17}$$

We can then see how q is relaxed to A in the time scale of τ from Equation (1.17). The thermal relaxation time for biological tissues has typically been found to be large, leading to significant non-Fourier thermal behavior. Mitra et al. [44] conducted an experiment in which they measured the thermal relaxation time in processed meat and reported that τ could be as large as 16 s. Kaminski [40] reported that τ ranges from 10 to 50 s in his experiment with materials with inhomogeneous inner structures. Roetzel et al. [48] also confirmed the hyperbolic behavior of thermal propagation with τ about 1.77 s in a similar experiment. Using the thermal properties of tissue and blood from some literatures, Zhang [49] computed and argued that reasonable τ should range from 0.464 to 6.825 s. He further found that the dual-phase lag phenomenon in temperature and its gradient due to the wave feature is more pronounced when the blood vessel is large. Shih et al. [33] continued to explore the heat wave caused by thermal relaxation time and further investigated the coupled effect of blood flow in large blood vessels and thermal relaxation time on the heating of tumor tissues. Based on the results of Shih et al. [33], we discuss the related heat wave behavior caused by non-zero thermal relaxation time.

1.3.2 Mathematical Model and Numerical Method

1.3.2.1 Features of the Hyperbolic Heat Equation

Consider the 1D transient heat equation without any heat source as follows:

$$\rho c_{\mathrm{p}}\frac{\partial T(x,t)}{\partial t} + \frac{\partial q(x,t)}{\partial x} = 0, \tag{1.18}$$

with ρ being the density and c_{p} being the specific heat. Differentiating Equation (1.18) with respect to t, and multiplying it by τ, we can obtain a new equation. Adding this new equation to Equation (1.18), and applying Equation (1.16), we can obtain the following hyperbolic heat equation:

$$\rho c_{\mathrm{p}}\tau\frac{\partial^2 T}{\partial t^2} + \rho c_{\mathrm{p}}\frac{\partial T}{\partial t} = k\frac{\partial^2 T}{\partial x^2}, \tag{1.19}$$

or

$$\frac{\partial^2 T}{\partial t^2}+\frac{1}{\tau}\frac{\partial T}{\partial t}=c^2\frac{\partial^2 T}{\partial x^2}, \tag{1.20}$$

with the wave speed $c=\sqrt{\frac{k}{\rho c_p \tau}}$. Here we conduct a normal mode analysis of Equation (1.20) by studying its solution form in traveling wave $T(x,t)=e^{i(\xi x-\omega t)}$. Substituting this traveling wave solution into Equation (1.20), we can obtain its dispersion relationship:

$$\omega=\frac{-i\pm\sqrt{4\tau^2c^2\xi^2-1}}{2\tau}, \tag{1.21}$$

and then

$$T(x,t)=e^{-\frac{t}{2\tau}}e^{i\xi(x-c_{\text{eff}}t)},\quad c_{\text{eff}}=\pm\frac{\sqrt{4\tau^2c^2\xi^2-1}}{2\xi\tau},\quad \text{when } 4\tau^2c^2\xi^2\geq 1, \tag{1.22}$$

$$T(x,t)=e^{\left(\frac{-1\pm\sqrt{1-4\tau^2c^2\xi^2}}{2\tau}\right)t}e^{i\xi x},\quad \text{when } 4\tau^2c^2\xi^2<1. \tag{1.23}$$

From Equation (1.22), high-frequency modes travel in two directions and damp at the same time, while low-frequency modes simply decay without propagation from Equation (1.23). The attenuation rate decays with increasing τ for both high-frequency and low-frequency modes. All these mean that while temperature is decaying as a whole, we can only observe high-frequency waves traveling.

1.3.2.2 *Thermal Governing Equations and the Numerical Method*

Here we consider the same geometric configuration and blood velocity profile (Equation 1.10) as in Section 1.2. Usually, the governing equations for the temperature evolution are the PBHTE shown in Equation (1.24) for solid tissue and energy transport equation shown in Equation (1.25) for blood flow in terms of the cylindrical coordinate under an axis-symmetric situation:

$$\rho_t c_t\frac{\partial T_t}{\partial t}=k_t\left[\frac{1}{r}\frac{\partial}{\partial r}\left(r\frac{\partial T_t}{\partial r}\right)+\frac{\partial^2 T_t}{\partial z^2}\right]-W_b c_b(T_t-T_a)+Q_t(r,z,t), \tag{1.24}$$

$$\rho_b c_b\left(\frac{\partial T_b}{\partial t}+W\frac{\partial T_b}{\partial z}\right)=k_b\left[\frac{1}{r}\frac{\partial}{\partial r}\left(r\frac{\partial T_b}{\partial r}\right)+\frac{\partial^2 T_b}{\partial z^2}\right]+Q_b(r,z,t), \tag{1.25}$$

with symbol of notations and meaning of each term the same as in Section 1.2.

Taking into account the finite thermal propagation speed in living solid tissues, we modified Equation (1.24) by the heat flux formula in Equation (1.16) following the same procedure used to arrive at Equation (1.19), and obtained a hyperbolic bioheat transfer equation (HBTE) as shown in Equation (1.26) to replace Equation (1.24):

$$\rho_t c_t\left(\tau_t\frac{\partial^2 T_t}{\partial t^2}+\frac{\partial T_t}{\partial t}\right)=k_t\left[\frac{1}{r}\frac{\partial}{\partial r}\left(r\frac{\partial T_t}{\partial r}\right)+\frac{\partial^2 T_t}{\partial z^2}\right]+W_b c_b(T_a-T_t)+Q_t+\tau_t\left(-W_b c_b\frac{\partial T_t}{\partial t}+\frac{\partial Q_t}{\partial t}\right), \tag{1.26}$$

in which the terms on the left side represent heat wave and heat diffusion, respectively. They are competing with each other with the thermal relaxation time τ_t characterizing the strength of wave. When $\tau_t = 0$, HBTE (Equation 1.26) will totally reduce to a parabolic-type PBHTE (Equation 1.24), and heat wave reduces to heat diffusion. The external heating rate Q_t in Equation (1.26) and Q_b in Equation (1.25) are designated as follows:

$$Q_t(r,z,t) = \begin{cases} \widetilde{Q}_t \dfrac{\pi}{2} \sin\left(\dfrac{\pi_t}{t_h}\right), & r_0 \le r \le r_1, z_1 \le z \le z_2, 0 \le t \le t_h, \\ 0, & (r,z,t) \text{ otherwise}, \end{cases}$$

$$Q_b(r,z,t) = \begin{cases} \widetilde{Q}_b \dfrac{\pi}{2} \sin\left(\dfrac{\pi_t}{t_h}\right), & r \le r_0, z_1 \le z \le z_2, 0 \le t \le t_h, \\ 0, & (r,z,t) \text{ otherwise}, \end{cases} \tag{1.27}$$

where $\widetilde{Q}_t$ and $\widetilde{Q}_b$ are the time averaged values of Q_t and Q_b, respectively, and t_h is the duration of time of heating. In the study of this section, we let $\widetilde{Q}_t = \widetilde{Q}_b = Q$. Six heating schemes consisting of various combinations of Q and t_h are shown in Table 1.4, and schemes I-V are particularly employed here to study the effect of heating rate.

The initial conditions for the blood vessel and the tissue are

$$T_t(r,z,0) = T_b(r,z,0) = 37, \quad \text{and} \quad \frac{\partial T_t}{\partial t}(r,z,0) = 0^\circ\text{C/s}.$$

At the interface $\Gamma(r = r_0, 0 \le z \le z_{max})$ between the blood vessel and tissue, temperature and heat flux continuity conditions are imposed:

$$T_t = T_b, \quad \text{and} \quad k_t \frac{\partial T_t}{\partial n} = k_b \frac{\partial T_b}{\partial n} \quad \text{at } \Gamma,$$

where n denotes the direction normal to Γ. At $r = 0$, the pole condition was applied for the blood vessel:

$$\frac{\partial T_b}{\partial r} = 0.$$

The boundary conditions at $r = r_{max}, z = 0$, and $z = z_{max}$ are all set to:

$$T_t = T_b = 37^\circ\text{C},$$

except that the convective boundary condition is employed for the blood vessel part at $z = z_{max}$:

$$\frac{\partial T_b}{\partial t} + W \frac{\partial T_b}{\partial z} = 0, \quad \text{at } z = z_{max}.$$

Together with these initial boundary and interface conditions, Equations (1.25) and (1.26) were numerically solved by the highly accurate, multiblock Chebyshev pseudospectral method under the framework of MOL. Again, the computational domain is decomposed

to nine blocks, and designation of heating zones is the same as Section 1.2. For further numerical details, see Horng et al. [29] and Shih et al. [33].

1.3.3 Results and Discussions

Here we discuss how the thermal relaxation time τ_t affects the thermal treatment. Numerical experiments were conducted under exhaustive combinations of heating rate Q (first five schemes listed in Table 1.4), and thermal relaxation time ($\tau_t = 0, 0.464, 1.756,$ and 6.825 s as suggested in [49]). Here we only consider the case of the blood vessel diameter being 2 mm in Table 1.3, because larger blood vessels have been proved to be more thermally significant with sensitivity to heating rate [29]. The time evolution of maximum temperature and the thermal dose are particularly chosen here to demonstrate the effect of the thermal relaxation time. Though we did consider the blood flow to be pulsatile as periodically driven by the heart as in Section 1.2 in the beginning, blood flow pulsation was found to make negligible difference when just considering blood flow to be simply steady axial Hagen-Poiseuille flow, both in the time evolution of maximum temperature and thermal dose for all heating rates and τ_t considered here. We can, therefore, conclude that the thermal behavior is actually quite insensitive to the pulsation of blood flow [33].

The wave feature in HBTE (Equation 1.26) with large τ_t is found to be most pronounced when the heating rate is fast. In Figures 1.7 and 1.8, we compare the time evolution of the temperature distribution for $\tau_t = 0$ and 6.825 s under the case of the fastest heating rate (heating scheme I in Table 1.4). A non-smooth temperature distribution in space is clearly observed during time evolution in Figure 1.8 for $\tau_t = 6.825$ s, featuring high-frequency wave propagating, while only smooth temperature distribution is observed all the time in Figure 1.7 for $\tau_t = 0$ s, featuring the parabolic tendency of PBHTE in Equation (1.24). Notice that only high-frequency waves are pronounced in Figure 1.8. This is because high-frequency modes propagate and at the same time attenuate, while low-frequency modes attenuate only. This can be well explained by the analysis in Section 1.3.2.1.

The time evolution of the maximum temperature in space, $\max_{(r,z)\in\Omega} T$, can be particularly useful to demonstrate the effect of thermal relaxation time under different heating rates as shown in Figure 1.9. Generally, this maximum temperature happens near the center of zone 5 (tumor tissue). For $\tau_t = 0$, we can see $\max_{(r,z)\in\Omega} T$ always reaches its maximum in time right at the end of heating as expected, while $\max_{(r,z)\in\Omega} T$ generally exhibits a plateau in time after the end of heating for non-zero τ_t's, which is more pronounced as τ_t is large and heating rate is fast by comparing sub-figures in Figure 1.9. This can be easily understood by the larger lagging of heating and smaller attenuation rate from Equation (1.23) for low-frequency modes when τ_t is large. Obviously, high temperature also tends to accumulate and preserve in time at the tumor zone when the heating is fast (less time for tumor to respond and relax thermally). Notice that, for slow heating in Figure 1.9d and e, the maximum temperature plateau is far less pronounced compared with fast heating in Figure 1.9a-c and this is because the heating is so slow that the tumor has enough time to respond and relax thermally. In Figure 1.9d and e, we can also observe non-zero τ_t's even lead $\tau_t = 0$ in time to reach their maxima, and the larger τ_t's are, the larger maxima are reached. Again, this can be explained by the larger heating lagging and less attenuation as τ_t gets large.

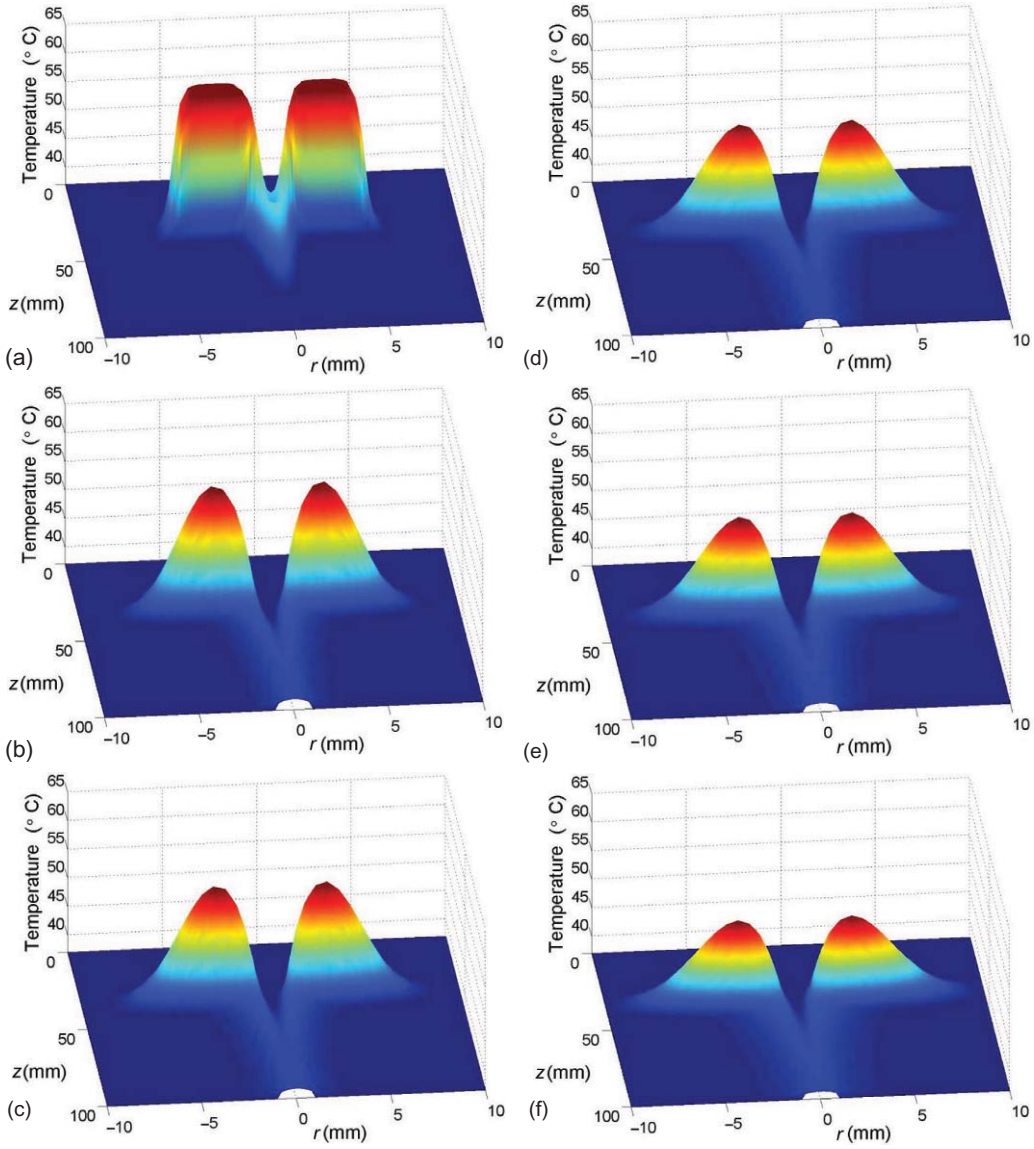

FIGURE 1.7 Time development of temperature distribution in space for $\tau_t = 0$ s under heating scheme I in Table 1.4 of Section 1.2 is shown at (a) $t = 1$ s, (b) $t = 7.5$ s, (c) $t = 10$ s, (d) $t = 12$ s, (e) $t = 14.5$ s, (f) $t = 19.5$ s. The blood vessel diameter is 2 mm.

From Figure 1.10, we can observe that the tumor tissue is generally covered better by a thermal lesion region based on $EM_{43} = 240$ min level curve when heating is fast, and that this effect is further enhanced when τ_t is large. Some of these regions even cover a small part of the normal tissue near the downstream junction of the blood vessel, tumor, and normal tissue as shown in Figure 1.10a and b, which is actually not desired in thermal treatment.

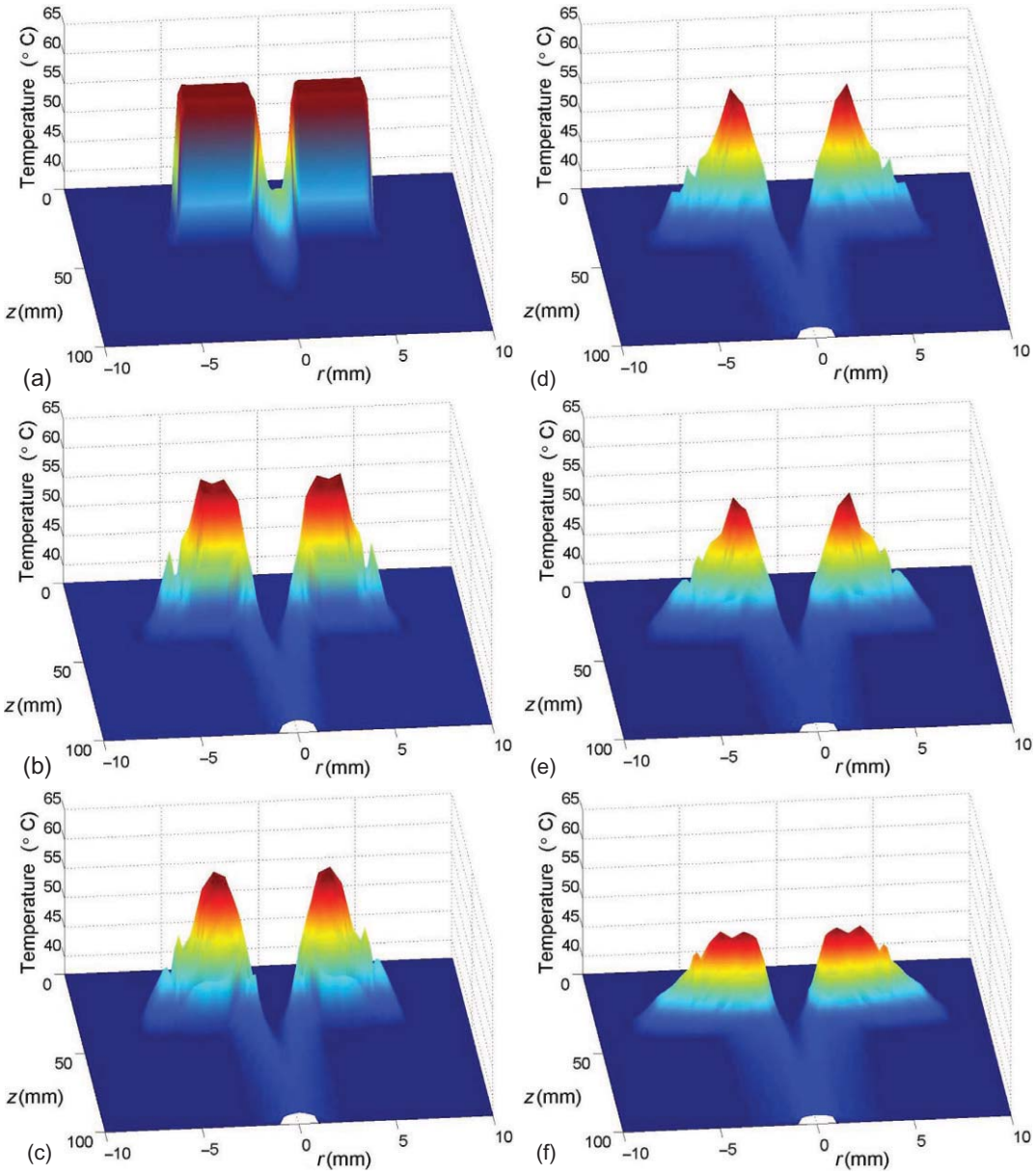

FIGURE 1.8 Time development of temperature distribution in space for $\tau_t = 6.825$ s under heating scheme I in Table 1.4 of Section 1.2 is shown at (a) $t = 1$ s, (b) $t = 7.5$ s, (c) $t = 10$ s, (d) $t = 12$ s, (e) $t = 14.5$ s, (f) $t = 19.5$ s. The blood vessel diameter is 2 mm.

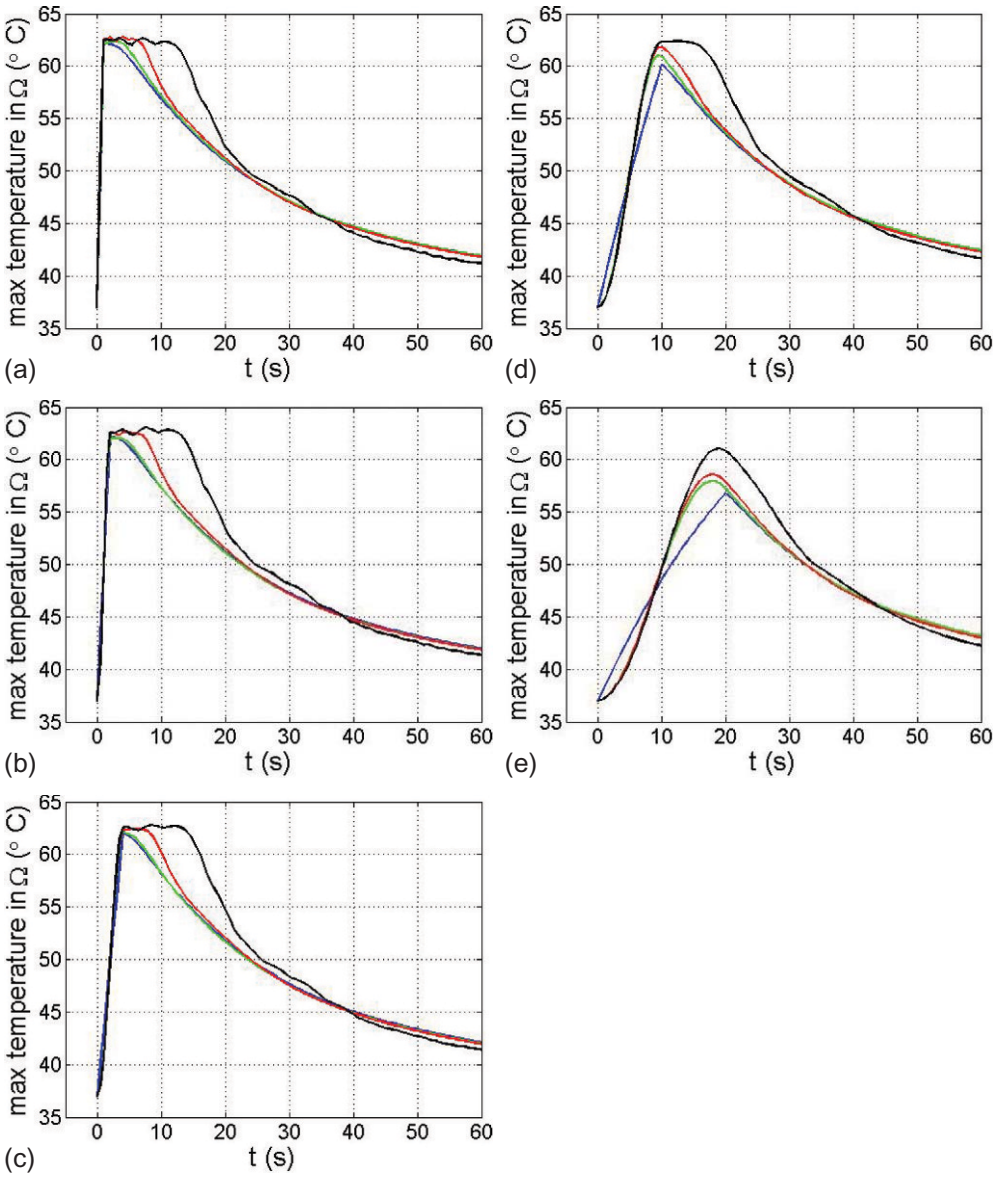

FIGURE 1.9 Maximum temperature in space $\max_{(r,z)\in\Omega} T$ versus time with heating schemes I-V in Table 1.4 in Section 1.2 shown in (a-e), respectively. $\tau_t = 0, 0.464, 1.756,$ and 6.825 s are represented by blue, green, red, and black curves, respectively. The blood vessel diameter is 2 mm.

The phenomenon above is comprehensible from the fact that the high temperature is preserved for longer durations and the heat is drained more slowly when heating is fast and τ_t is large (as demonstrated in Figure 1.9). Generally speaking, the traditional simulations based on PBHTE may underestimate the thermal lesion region by neglecting nontrivial thermal relaxation time in living tissues.

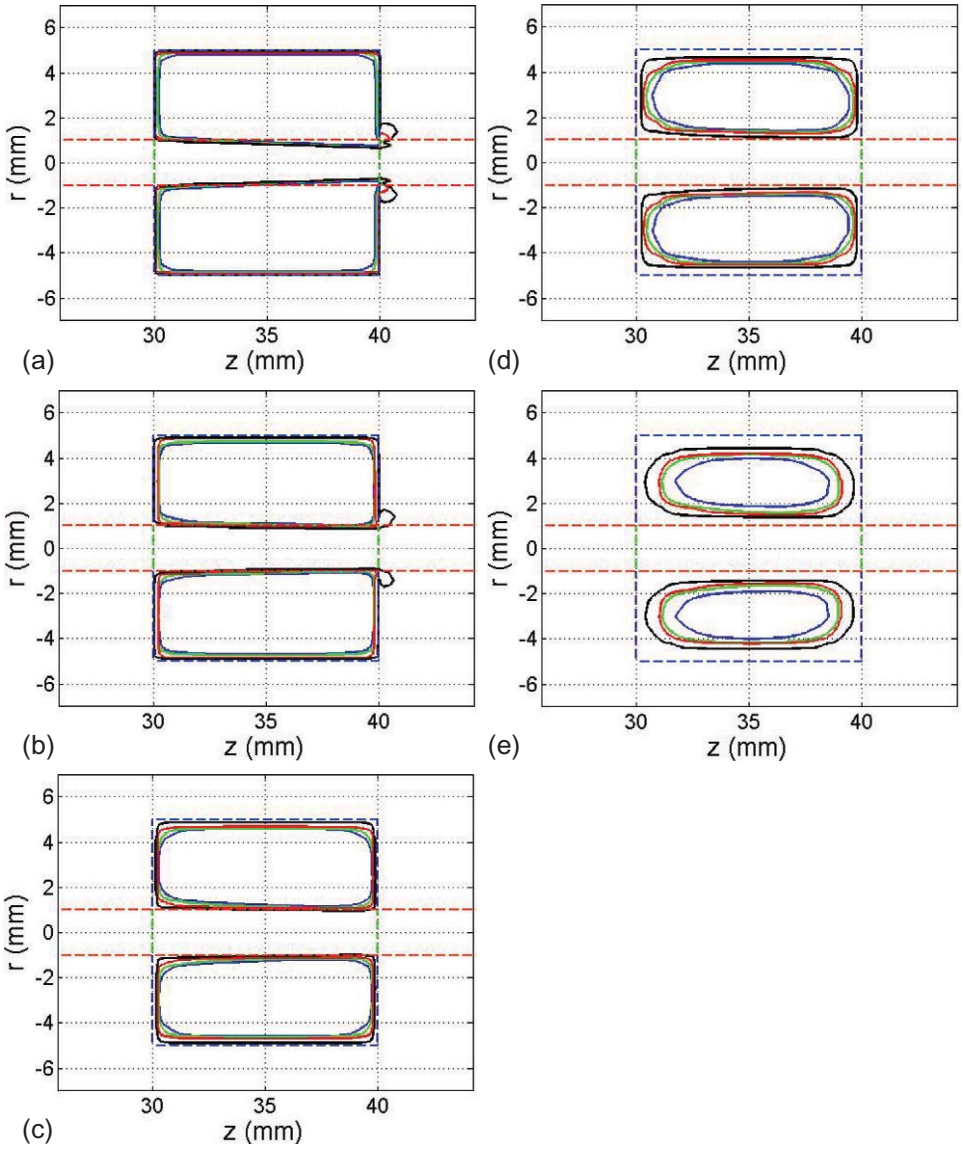

FIGURE 1.10 Thermal lesion region represented by $EM_{43} = 240$ min contour with heating schemes I-V in Table 1.4 of Section 1.2 shown in (a-e), respectively. $\tau_t = 0, 0.464, 1.756$, and 6.825 s are represented by blue, green, red, and black curves, respectively. The blood vessel diameter is 2 mm.

1.3.4 Conclusion

From the coupling model of thermal hyperbolic bioheat transfer in solid tissues and energy transport of blood flow in thermal significant blood vessels developed above, the thermal behavior is found to be very sensitive to the heating rate and the thermal relaxation time. Heat leaves the target region more slowly and tumor tissue preserves high temperature longer

when heating is fast and thermal relaxation time is large. This is all due to the larger lagging of heating and less attenuation for low-frequency modes as τ_t gets large. The wave feature characterized by large thermal relaxation time also causes the thermal lesion region based on $EM_{43} = 240$ min level curve to cover the tumor region better. It implies that the traditional simulations based on PBHTE may underestimate thermal dose because thermal relaxation time is actually nontrivial in living tissues.

1.4 PBHTE WITH THE VASCULAR COOLING NETWORK MODEL

As stated in the previous section, blood flow accounts for up to 90% of heat removal [50]. Thus, attempting to model complicated vascular geometry in which blood circulates along those different sizes of vessels is an important approach to analyze precisely the heat transfer processing in a biothermal system. To account for the impact of large blood vessels on the heat transfer processes, thermal models have to take conductive and convective heat transport into account. And many researchers have attempted to describe the impacts of the blood vessels [18]. Some of the vascular models have been designed not for application in hyperthermia treatment planning, but to obtain basic insight into the heat transfer between large blood vessels and tissue. Therefore, these models are relatively simple with straight vessels represented by a tube with a specified diameter [16,51–53]. These basic models are also very useful in calculating the temperature distributions induced by thermal ablation, where it is necessary to account for a single large blood vessel passing through a target region. The heat transfer modes—conduction and convection—are seen during biological processes. Investigation of the basics of heat transfer using basic discrete vessel models and a selection of these models are discussed below.

1.4.1 Thermally Significant Blood Vessel Model

During the late 1980s, many investigators [9–11], following the rationale that was similar to that which initiated the CH and WJ models presented in Section 1.1, began to question the handling of the blood perfusion term and how to better approximate the blood temperature and the local tissue temperatures where blood vessels (countercurrent vessels) are involved. Because arterial and venous capillary vessels are small, their thermal contributions to local tissue temperatures are insignificant when compared with large blood vessels. However, for vessel sizes larger than the capillaries, there are noticeable, thermally significant impacts on the local tissue temperatures during either the cooling or heating processes. Several investigators [16,51] examined the effect of large blood vessels on the temperature distribution using theoretical studies. Huang et al. [54], in 1996, presented a more fundamental approach to model temperatures in tissues than do the generally used approximate equations, such as the PBHTE or effective thermal conductivity equations. As such, this type of model can be used to study many important questions at a more basic level. For example, in the particular hyperthermia application studied [54], a simple vessel network model predicts that the role of countercurrent veins is minimal and that their presence does not significantly affect the tissue

temperature profiles. The arteries, however, removed a significant fraction of the power deposited in the tissue. The Huang model used a simple convective energy balance equation to calculate the blood temperature as a function of position:

$$\dot{M}_i c_b \frac{dT_b}{dx_i} = \dot{Q}_{ap} - h_i A_i (T_b - T_w). \tag{1.28}$$

Here, $\dot{M}_i$ is the mass flow rate of blood in artery i, c_b is the specific heat of blood, $T_b(x_i)$ is the average blood temperature at position x_i, x_i indicates the direction along the vessel i (either x, y, or z depending on the vessel level). $\dot{Q}_{ap}$ is the applied power deposition, x_i is the position x along blood vessel i, h_i is the heat transfer coefficient between the blood and the tissue, A_i is the perimeter of blood vessel i, and $T_w(x_i)$ is the temperature of the tissue at the vessel wall. For the smallest, terminal arterial vessels, a decreasing blood flow rate is present, resulting in the energy balance equation:

$$\dot{M}_i c_b \frac{dT_b}{dx_i} = \dot{Q}_{ap} - h_i A_i (T_b - T_w) - \frac{d\dot{M}_i}{dx_i} c_b T_b. \tag{1.29}$$

The blood leaving these terminal arterial vessels at any cross-section is assumed to perfuse throughout the tissue at a constant rate. A detailed description is given by Huang et al. [54]. As to the venous thermal model, for all veins except the smallest terminal veins, Equation (1.28) holds. For the smallest veins, the blood temperature, T_b, is replaced by the venous return temperature, $T_{vr}(x_i)$. In the presented study, this temperature is taken to be the average temperature of four tissue nodes adjacent to the terminal vein in the plane perpendicular to that vein:

$$T_{vr} = \frac{1}{4} \sum_{i=1}^{4} T_{i,adj}, \tag{1.30}$$

$T_{i,adj}$ is the tissue temperatures adjacent to the venous vessel. As a terminal vessel runs in any x, y, or z straight direction, there are four neighboring tissue nodes considered in terms of the computational scheme (i.e., finite difference method). In order to graphically illustrate the models and assumptions above, Figure 1.11 shows models depicting Equations (1.28)–(1.30).

1.4.2 Vessel Network Geometry and Fully Conjugated Blood Vessel Network Model

The Fully Conjugated Blood Vessel Network Model (FCBVNM) is a model formulation which describes the solid tissue matrix having thermally significant vessel generations (seven levels) by Huang et al. [54]. The effects of all vessels smaller than the terminal (level 7) vessels are not explicitly modeled in FCBVNM. Thus, those smaller vessels (connected to the terminal arteries and the terminal veins in the network) are implicitly assumed to be thermally insignificant in the FCBVNM.

The tissue geometry used in this study [54] consists of a regular, branching vessel network as partially shown (only the arterial vessels are shown) in Figure 1.12 that is embedded in a

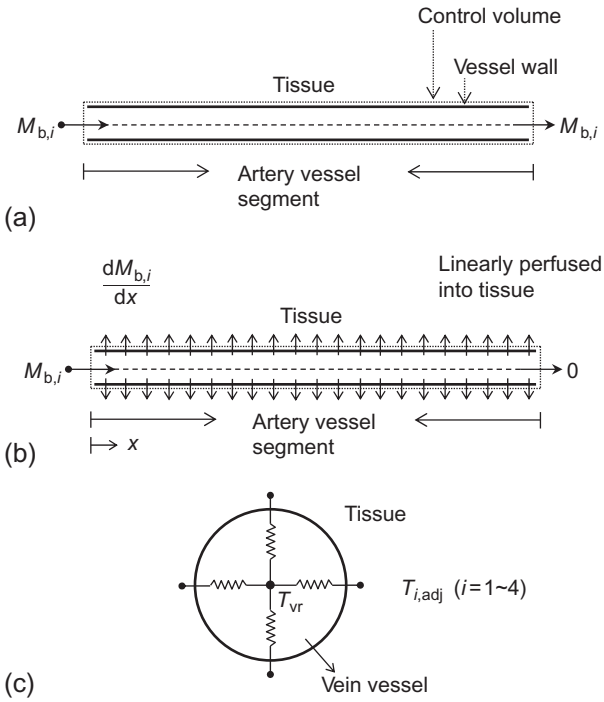

FIGURE 1.11 (a) The model used for nonterminal artery blood vessels in which the convective energy Equation (1.28) is solved for the FCBVNM model. $M_{b,i}$ is the blood flow rate entering vessel i and leaving with an identical mass flow rate $M_{b,i}$. (b) The model used for the artery terminal vessels (level 7) as explained in Equation (1.29). $M_{b,i}$ is the blood flow rate entering vessel i with a linearly perfused mass flow rate into tissue of $dM_{b,i}/dx$. (c) The model calculating returning vein blood temperature, as explained in Equation (1.30).

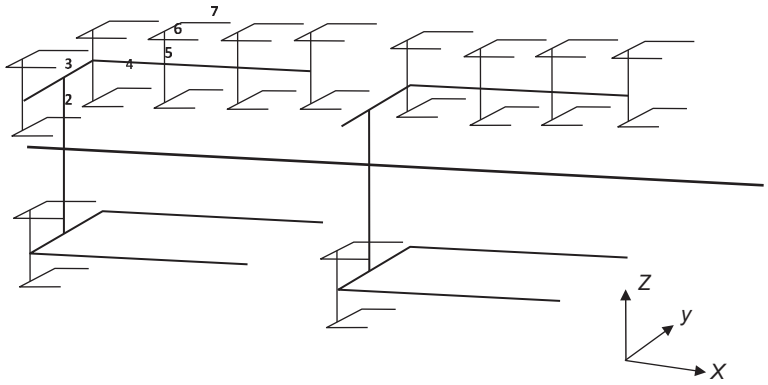

FIGURE 1.12 Schematic diagram to show a portion of the arterial vessel network used in this study. All seven vessel levels (level 1-7) for the arterial network are shown, and the venous network, which is not shown, is parallel to the arterial network, with a grid size in the x, y, and z dimensions away from the arterial network. '1' is not shown in Fig 1.12. It represents the main artery (level 1) and largest artery of 7-level blood vessel model. The level 1 artery lies along the long central, lengthwise (x) axis in Fig.1.12.

control volume, which is an (approximate) cube of dimensions $L=8.2$ cm and $W=H=8$ cm in the x, y, and z directions, respectively. All vessels are straight-line segments and are parallel to one of the three Cartesian axes. There are up to seven levels of arteries, beginning with the main artery (level 1) which lies along the central, lengthwise (x) axis of the cube. Table 1.5

TABLE 1.5 Vascular Parameters for Each Vessel Level in the Vascular Network

Vessel level	Total number of vessels	Individual vessel length	Vessel diameter	Vessel spacing (x, y, z)	Maximum mass flow rate in vessel	Total vessel surface area
1	1	$L/2$[a]	D	NA	128 $PV_{tsv}+M_{TA}$[b]	$\pi LD/2$
2	4	$H/4$	γD	NA, NA, $L/2$	32 PV_{tsv}	$\gamma\pi HD$
3	8	$W/4$	$\gamma^2 D$	NA, $H/2$, $L/2$	16 PV_{tsv}	$2\gamma^2\pi WD$
4	8	$3L/8$[c]	$\gamma^3 D$	$W/2$, $H/2$, NA	12 PV_{tsv}	$3\gamma^3\pi LD$
5	64	$H/8$	$\gamma^4 D$	$W/2$, NA, $L/8$	2 PV_{tsv}	$8\gamma^4\pi HD$
6	128	$W/8$	$\gamma^5 D$	$W/4$, $H/4$, $L/8$	PV_{tsv}	$16\gamma^5\pi WD$
7	128	$L/8-\Delta$[d]	$\gamma^5 D$	$W/4$, $H/4$, NA	PV_{tsv}	$16\gamma^5\pi(L-8\Delta)D$

NA indicates that the particular parameter in not applicable for that vessel level.
[a] *The level 1 vessel terminates at the center of the control for all cases* i *in this paper.*
[b] *The value at the inlet to the control volume.*
[c] *Each level 4 vessel has three segments.*
[d] *The terminal ends of one set of level 7 vessels are separated from the beginning of the next set of level 7 vessels by a gap of one finite difference nodal space,* $\Delta=2$ *mm.*

lists the basic vessel network properties used in this section (vascular parameters for each vessel level in the vascular network model in simulation). The diameters of the arteries decrease by a constant ratio, γ, between successive levels of branching vessels (the ratio of diameters of successive vessel generations), in other words:

$$\gamma=\frac{D_{i+1}}{D_i}, \tag{1.31}$$

where D_i and D_{i+1} are the diameters of two successive levels of branching arteries. When two successive levels of numbered vessels do not branch but only change direction (i.e., levels 6 and 7 in this model), the vessel diameter does not change. In this study, we used $\gamma=0.9$ in the presented results.

The desired treated tumor region is a cube described in Figure 1.13a with 20 mm in x, y, and z dimensions. The locations and paths of arterial vessels inside the treated region are described in Figure 1.13b and c. The geometric arrangement of the countercurrent veins is essentially identical to that of the arteries, with all of the veins offset from the arteries by one finite difference node in x, y, and z dimensions as appropriate to avoid intersections of vessels.

1.4.3 Discrete Vessel Modeling with Semicurved Vessel Network and Real 3D Vasculature Network

A vasculature model with straight lines provides a tool for a better analysis in a heat transfer process that is influenced by convection from different sizes of vessels. A more flexible algorithm in which the model geometry is subdivided into a vessel space and a tissue space has been developed by Mooibroek and Lagendijk [55] to obtain a more realistic, semicurved representation of vessel networks for use in hyperthermia treatment planning. This semicurved

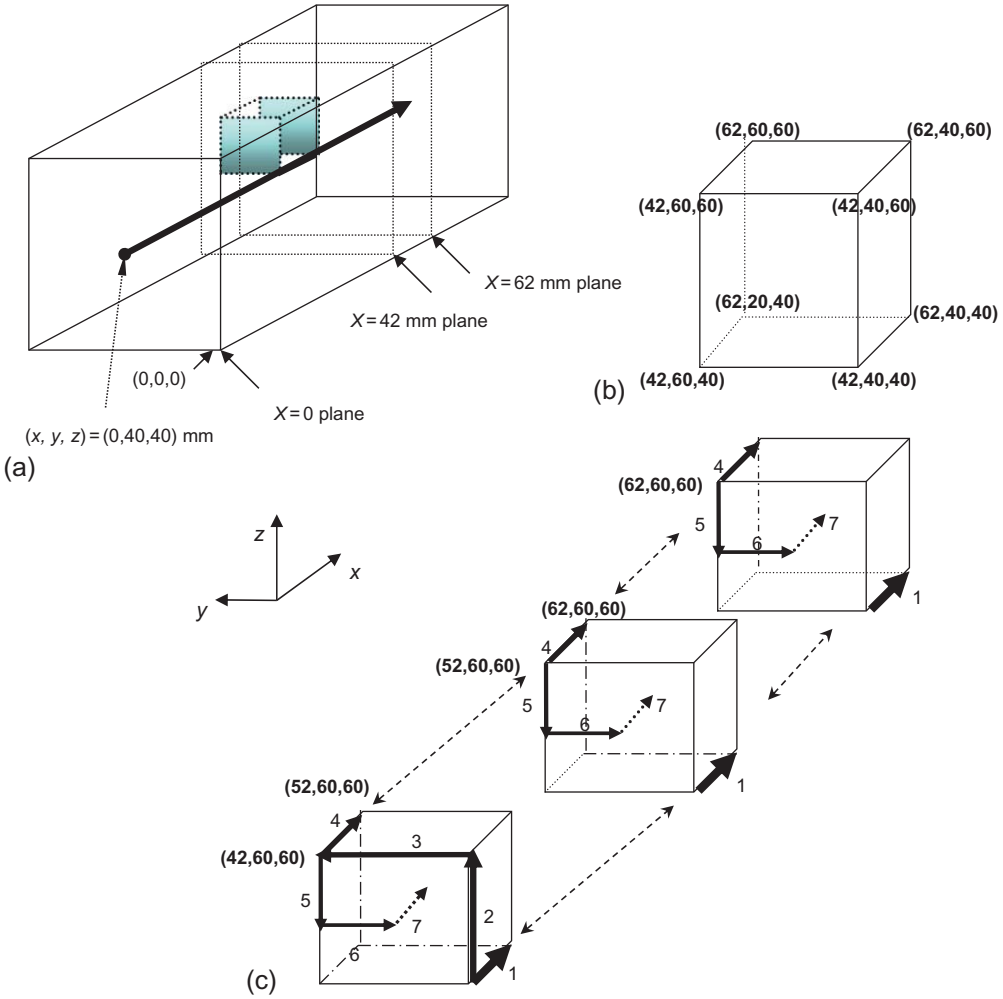

FIGURE 1.13 (a) A transparent view of parallelepiped showing the desired heated tumor region, which is a cube of 20 mm in each dimension. The level 1 blood vessel (largest) runs through the desired heated cube's edge from (42, 40, 40) to (62, 40, 40). The inlet temperature of the level 1 vessel starting at (0, 40, 40) is set at 37 °C. (b) Shows the coordinates of eight corners of the desired treated cube (unit: mm). (c) Is a dissected transparent view showing all associated arterial blood vessel paths (or segments) in the cubic volume, and venous vessels do not appear in the figure. There are two branches of level 5-7 blood vessels and one of level 5 and 6 on the back boundary as the dissected view indicates.

model uses a finite difference method, and the vessel segments are represented by connected strings of vessel nodes. The nodes with their centers closest to the vessel axis are considered vessel nodes. The description of a 3D vessel segment is used as a building block, which allows modeling of realistic complex vessel networks. A vessel-specific second discretization step in time is performed to describe the convective heat transfer within the vessel space. This makes it possible to incorporate vessels with different flows and diameters. Furthermore, the predicted

thermal equilibration lengths were compared to theoretical values, and a reasonable agreement was observed. Comparison with phantom measurements showed accuracy within the range of the experimental error. This result shows that cylindrically shaped vessels can be modeled accurately using a square grid, which is a very important simplification for numerical techniques used by practitioners. However, because of the cubic subdivision of blood vessels, a one-to-one description of a true 3D vessel network cannot be realized with this model.

To address the above-mentioned problems, a more sophisticated thermal model that allows thermal modeling with real detailed 3D discrete vasculature networks (DIVA) has been developed by Kotte et al. [56,57]. Similar to Mooibroek and Lagendijk [55], the model geometry is subdivided into a vessel space and a tissue space, but in the DIVA model, the vasculature is described by 3D curves with a specified diameter. This approach allows the consideration of all relevant blood vessels independent of the voxel size. Besides the clear advantage of the tissue-voxel resolution independence, modeling blood vessels as 3D curves makes the model compatible with MR/CT (Magnetic Resonance/Computerized Tomography) angiography vessel reconstruction software, which is essential for routine use in treatment planning. As to the heat transfer calculation, the exact heat flow between a vessel segment and its surrounding tissue is difficult to calculate for a realistic situation with a heterogeneous vessel network that includes power and temperature distributions. To solve this problem, a method to estimate the heat flow using a simplified situation has been developed [56]. For a vessel segment embedded in a tissue cylinder, an analytical expression for the heat flow can be derived when cylindrically symmetric boundary conditions and a thermally fully developed flow are assumed. The latter is justified because the entrance length is considerably shorter than the equilibration length [18].

1.4.4 Conclusion

There has been substantial progress in thermal modeling with discrete vasculature. Many basic models have been developed to provide insight into the cooling effects of vasculature and temperature gradients around large blood vessels. Modeling of straight and semicurved vessel networks has led to improved characterization of heat transfer between vasculature and tissue. However accuracy and time efficiency will be great concerns when complicated vasculature thermal models are developed and used in the real time clinic treatments.

1.5 HYPERTHERMIA TREATMENT PLANNING

A treatment planning for hyperthermia in biological processes is essential for adequate treatment control. Reliable temperature information during clinical hyperthermia and thermal ablation must comprise a thermal model, but conventional temperature measurements do not provide 3D temperature information. The model must take conductive and convective heat transport into account, as blood flow plays a significant role in hyperthermia [50]. Hyperthermia cancer treatment requires precise thermal absorbed power deposition to raise tumor tissue temperature up to the therapeutic range with a sufficient amount of time duration to prevent overheating the normal tissues. Many researchers [58–61] have investigated a

noninvasive heating modality for exploring power deposition with fine spatial resolution and/or optimization within the tumor region. Hyperthermia applicator technology is currently one of the most important things that can improve temperature homogeneity in the treated region as well as help to reach an optimal applied power field. This section investigates the significance of blood vessels in the absorbed power and temperature distributions when optimization was employed during hyperthermia. The treated tumor region is simulated using a three-dimensional (3D) tissue model embedded with a countercurrent blood vessel network [54]. 3D absorbed power depositions are obtained by using optimization to reach a uniform temperature of 43 °C for the desired treated region. The results show that the absorbed power deposition for optimization with fine spatial resolution produces a uniform temperature distribution maintained at 43 °C in the desired treated tumor region except for some cold spots and/or small cold strips caused by thermally significant large vessels. The amount of total absorbed power suggests that a region with thermally significant vasculature requires much more power deposited than one without vasculature. In addition, optimization with coarse spatial resolution results in a highly inhomogeneous temperature distribution in the treated region due to the strong cooling effect of blood vessels. Therefore, prior to hyperthermia treatments, thermally significant blood vessels should be identified and handled carefully to effectively reduce their strong cooling effect, particularly those vessels flowing into the treated region.

1.5.1 Optimization with Fine Spatial Power Deposition: Based on Local Temperature Response in the Treated Region

Figure 1.14 is a flow chart describing continuously adjusting absorbed power deposition in the desired treated tumor region in order to reach ideal temperature (uniform temperature throughout the treated tumor region with a temperature of 43 °C). The evaluation criterion of absorbed power deposition is shown in Equation (1.32). It states that the root mean square of the difference between the ideal temperature (43 °C) and the calculated temperature of all heated target nodes which is normalized by the difference, 43-37 °C, reaches less than the criterion value (set to be 10% of the temperature difference of 43-37 °C). If this criterion is achieved, we obtain the optimization of absorbed power deposition such that the heating temperature distribution is close to the ideal temperature distribution. Otherwise, the absorbed power deposition will be adjusted according to the local temperature. The readjusted power deposition (P_{n+1}) is described in Equation (1.33):

$$\text{Evaluation criterion: } \frac{\sqrt{\dfrac{\sum_{\text{all target nodes}} (\Delta T(x,y,z))^2}{\text{Total number of target nodes}}}}{43-37\ ^\circ\text{C}} \le 0.1, \tag{1.32}$$

$$P_{n+1}(x,y,z) = P_n(x,y,z) + \Delta P(x,y,z), \tag{1.33}$$

with $\Delta P(x,y,z) = C \cdot \Delta T(x,y,z)$, C is 10,000, n is the iteration number, and $\Delta T(x, y, z)$ is the difference of ideal temperature (43 °C) and calculated temperature.

To investigate the significance of blood vessels in the temperature distribution for optimal hyperthermia treatment, an optimization scheme as described in Equations (1.32) and (1.33).

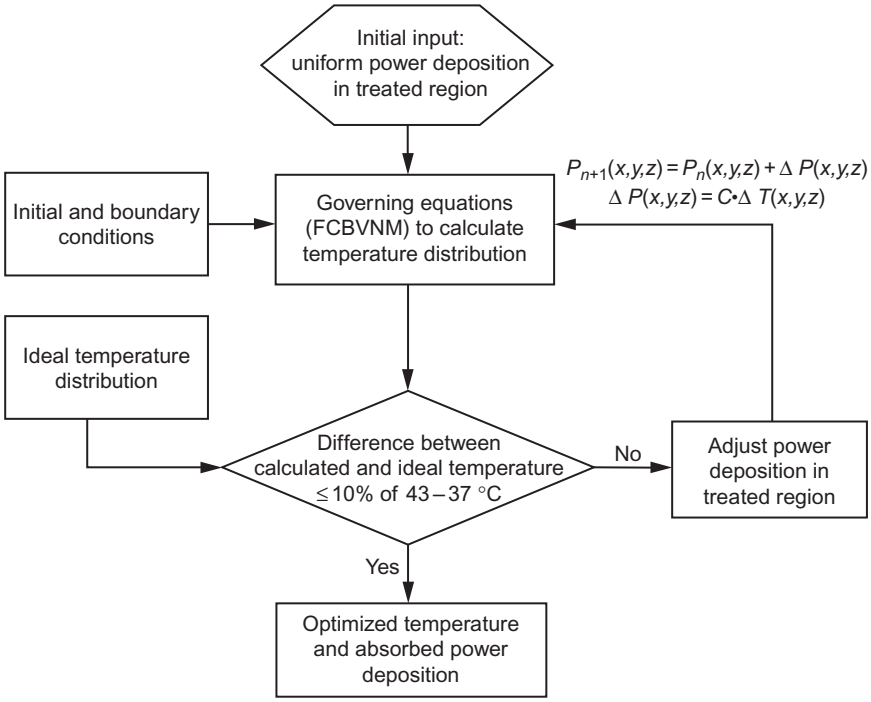

FIGURE 1.14 The flow chart of optimization used in this study. The absorbed power deposition in the desired treated cube (20 mm in each dimension) is adjusted locally in order to achieve an ideal therapeutic temperature of 43 °C uniformly for the entire cube.

The computational flow chart, shown in Figure 1.15, determines the absorbed power deposition, which includes the heating of blood vessels to achieve an optimal treatment. The flow chart to find the optimal solutions is used in this section. Figure 1.16a-e is the optimal temperature distributions on the planes 4 mm away from the front boundary, the middle, the back boundary, and 4 mm away from the back boundary of the treated region, respectively, and Figure 1.16f-h is the absorbed power depositions on the planes of the front boundary, the middle, and the back boundary of the treated region, respectively, for a blood perfusion of 0.5 kg/m^3/s and a blood flow velocity of 320 mm/s in the level 1 vessel. Figure 1.16a shows that the temperature is approximately 40.0 °C near the treated region and displays a cold spot at the center which is due to a level 1 artery blood vessel running perpendicular inwards to the plane. At its southeastern diagonal direction about 2.8 mm away from the level 1 artery, a level 1 vein is running in an opposite direction outwards to the plane. The vein appears to be collecting some thermal energy by convection through the treated region. Figure 1.16b shows that the temperature on the boundary of the treated region is close to ideal temperature (43 °C), and there are steep thermal gradients near the level 2 artery running upwards from the center point. As seen in Figure 1.16f, large amounts of thermal power were deposited on level 2, 3, and 5 arteries. The maximum thermal power deposition is approximately 3.7×10^6 W/m^3. Figure 1.16c shows that the temperature in the treated region is close to ideal

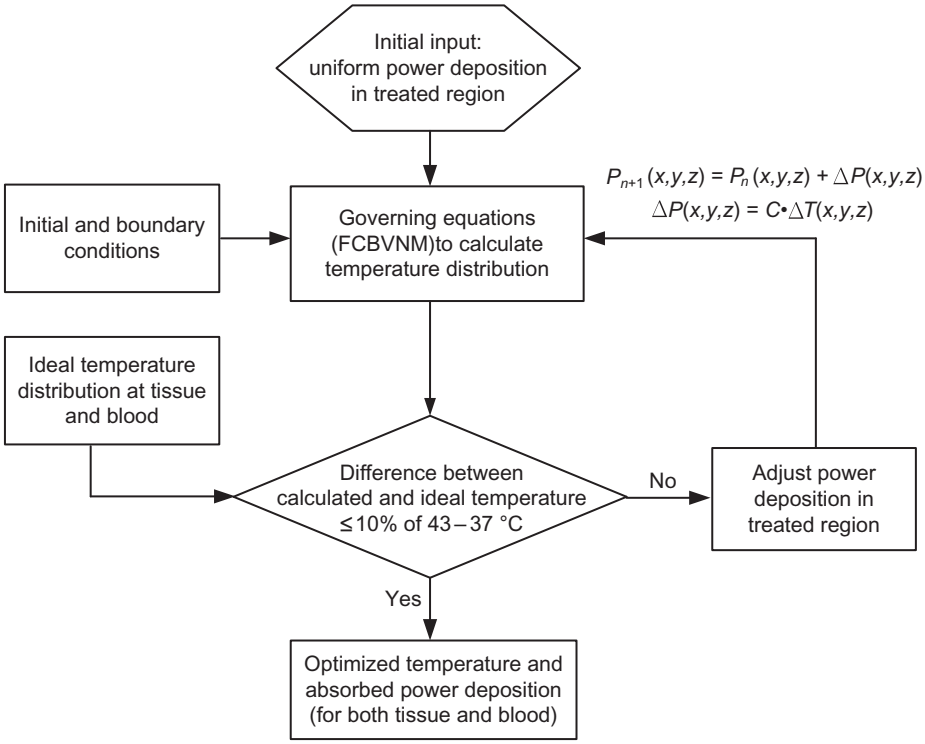

FIGURE 1.15 The computational flow chart to find the optimal power and temperature distributions during hyperthermia.

temperature, while high temperature appears outside of the treated region due to a level 6 artery carrying convective thermal energy leftwards. It illustrates that thermally significant blood vessels within the treated region have effectively been heated and carried the convective thermal energy out of the region. Figure 1.16c also shows maximum temperature located on (or near) the left-side artery branch node of level 5 and 6 arteries in the treated region. Figure 1.16g shows that large thermal power is deposited on the corner of the treated region, which is an area with dense blood vessels (level 3, 4, and 5 arteries and veins). In Figure 1.16d, the temperature distribution at the back boundary of the treated region shows that a cold spot is found near the northwestern corner of the heated region. The spot is 1.7 °C below the ideal temperature, and it is caused by the level 4 vein flowing into the heated region. As expected, Figure 1.16h shows a large amount of thermal power deposited on the same corner as shown in Figure 1.16g to compensate the heat loss caused by vessels. Dense blood vessels act as energy sinks, and a large amount of thermal power deposition is required in that area in order to maintain the local temperature at the desired level. Figure 1.16e, temperature on the plane 4 mm away from the back boundary of the heated region, shows some hot spots, and these spots are approximately 42 °C. One spot, located in the northeastern direction more than 4 mm away from the heated region, has a temperature of about 38.3 °C. Those hot spots are caused by arteries carrying hot blood flow.

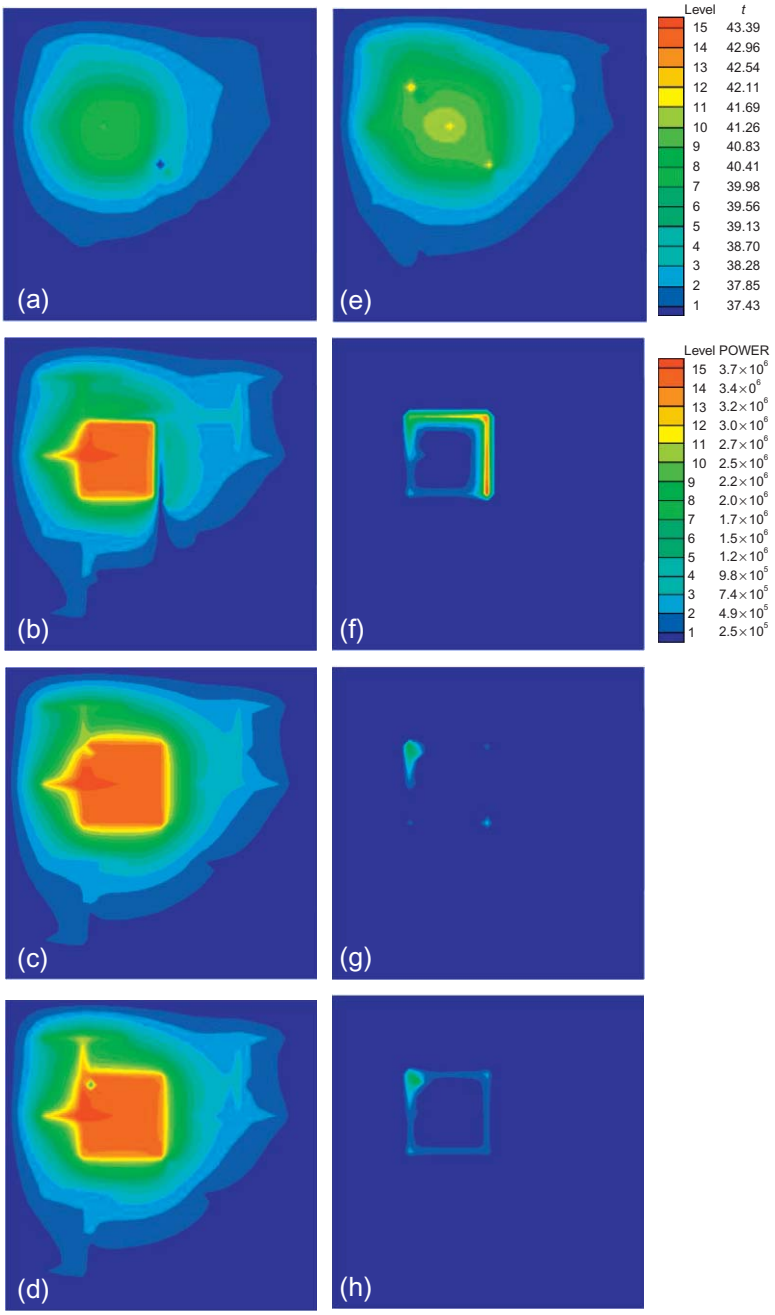

FIGURE 1.16 Temperatures and absorbed power depositions for a blood perfusion rate of 0.5 kg/m^3/s after optimization with fine spatial power deposition. The ideal temperature is set to be 43 °C, and the blood flow velocity is about 320 mm/s in level 1 vessel. (a-e) are the temperature distributions at $x=38$ mm (4 mm away from the front boundary), $x=42$ mm (the front boundary), $x=52$ mm (the middle of the treated region), $x=62$ mm (the back boundary), and $x=66$ mm (4 mm away from the back boundary) planes, respectively. (f-h) are the absorbed power depositions at $x=42$, 52, and 62 mm planes, respectively, after optimization (units in figure, t: °C and power: W/m^3).

1.5.2 Optimization with Lumped Power Deposition: Uniform Absorbed Power Deposition in the Treated Tumor Region

To investigate the spatial resolution of absorbed power deposition on the temperature distribution, a uniform power deposition in the entire desired treated tumor region is applied. Two important parameters need to be introduced for this optimization. One is cost function and the other is the power coefficient. Cost function at nth iteration is set to be $C_n = \sqrt{\sum_{\text{All target nodes}} (T(x,y,z) - 43^\circ\text{C})^2}$, with $\Delta C_{n+1} = C_{n+1} - C_n$, and the absorbed power is $P_{n+1} = P_n + h_{\text{coef}} \cdot \Delta C_n$ with the coefficient h_{coef}. h_{coef} is the updated power coefficient, with a constant value of 3050. It is chosen based on a smoothly converging (i.e., no oscillating) search and with less computational time required during optimization. The optimization process will be terminated when ΔC_n is smaller than 10^{-4}. Optimization of uniform power deposition allows the attention to be focused on the effect of the vasculature on the temperature distribution.

To investigate the effect of lumped power deposition on the resulting temperature distribution, a uniform power deposition for the entire treated region is used. This represents the limitation of the heating system to tune its power spatially fine enough to meet the treatment requirement. Figure 1.17a-e is the optimized temperature distributions on the planes of 4 mm away from the front boundary, the front boundary, the middle, the back boundary, and 4 mm away from the back boundary of the treated region, respectively, and Figure 1.17f-h is absorbed power depositions on the planes of the front boundary, the middle, and the back boundary, respectively, for a blood perfusion of 0.5 kg/m^3/s and a blood flow velocity of 320 mm/s in the level 1 vessel. The initial guess of the uniform power deposition in the treated region was 10^5 W/m^3, and the optimized absorbed power deposition was obtained as the difference (ΔC_n) between two successive cost function values was smaller than 10^{-4}. With this optimization of lumped power deposition, the temperatures shown in Figure 1.17b-d indicates that the temperatures in the treated region are highly inhomogeneous, with a temperature about 3 °C below the desired therapeutic temperature in the places near the boundary planes. These temperature distributions show that blood flow of vessels results in significantly lower temperature strips along the vessels in the treated region, particularly a large vessel located at the boundary of the treated region.

1.5.3 Effect of Blood Perfusion and Blood Flow Rates on the Optimization

As blood perfusion increases, the flow rates in vessels get higher due to the conservation of blood mass, and the higher flow rate will produce a stronger thermal impact on the treated region. Figure 1.18 shows temperature and power depositions for a blood perfusion of 2.0 kg/m^3/s and a blood flow velocity about 1280 mm/s in level 1 blood vessel. Figure 1.19 shows temperature and power depositions for a blood perfusion of 0.123 kg/m^3/s and a blood flow velocity of about 80 mm/s in a level 1 blood vessel, which in size and blood flow velocity of vessel is identical to dog data from CH [3]. The optimized power deposition pattern is similar to, but with a higher or lower value than, that shown in Figure 1.15, and the temperature distribution shows that uniform temperature close to the ideal value can be obtained in the

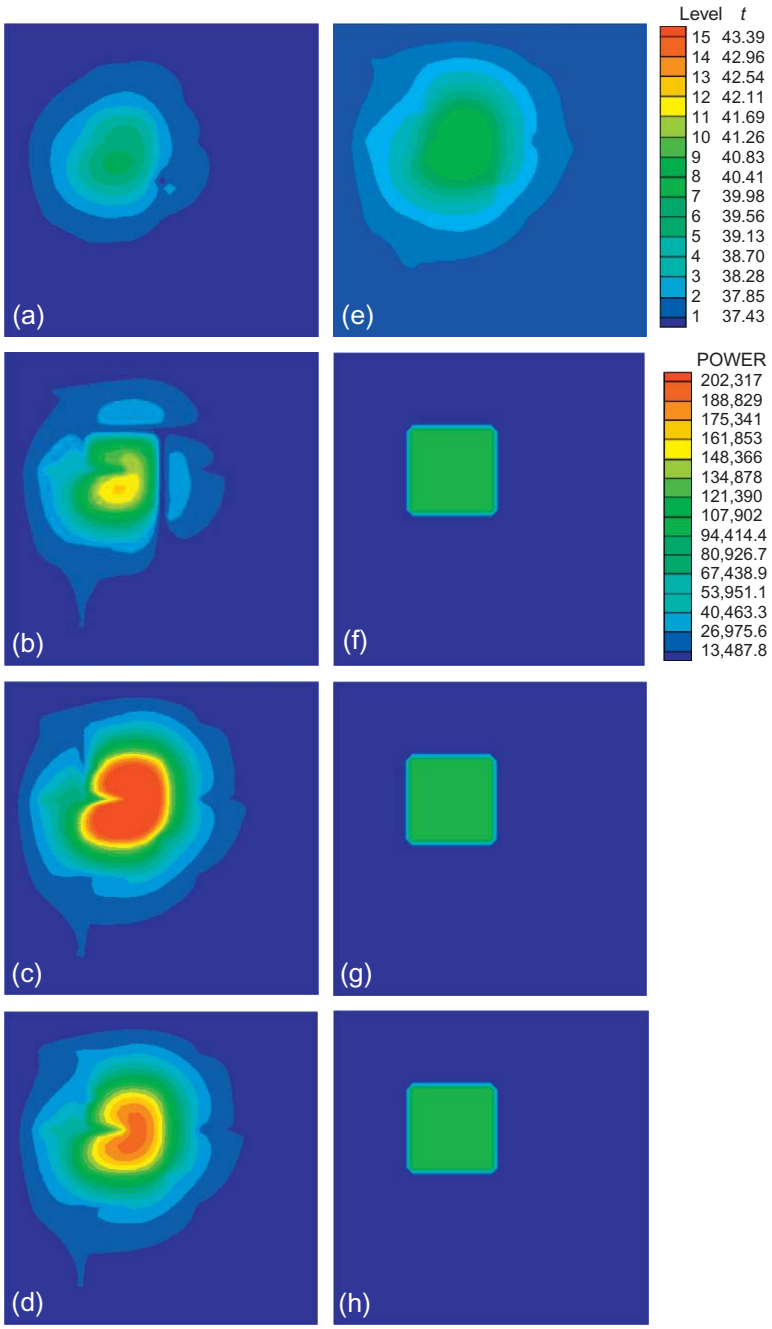

FIGURE 1.17 Temperatures and absorbed power depositions for a blood perfusion rate of 0.5 kg/m^3/s after optimization with lumped power deposition. The ideal temperature is set to be 43 °C, and the blood flow velocity is about 320 mm/s in level 1 vessel. (a-e) are the temperature distributions at $x=38$ mm (4 mm away from the front boundary), $x=42$ mm (the front boundary), $x=52$ mm (the middle of the treated region), $x=62$ mm (the back boundary), and $x=66$ mm (4 mm away from the back boundary) planes, respectively. (f-h) are the absorbed power depositions at $x=42$, 52, and 62 mm planes, respectively, after optimization (units in figure, t: °C and power: W/m^3).

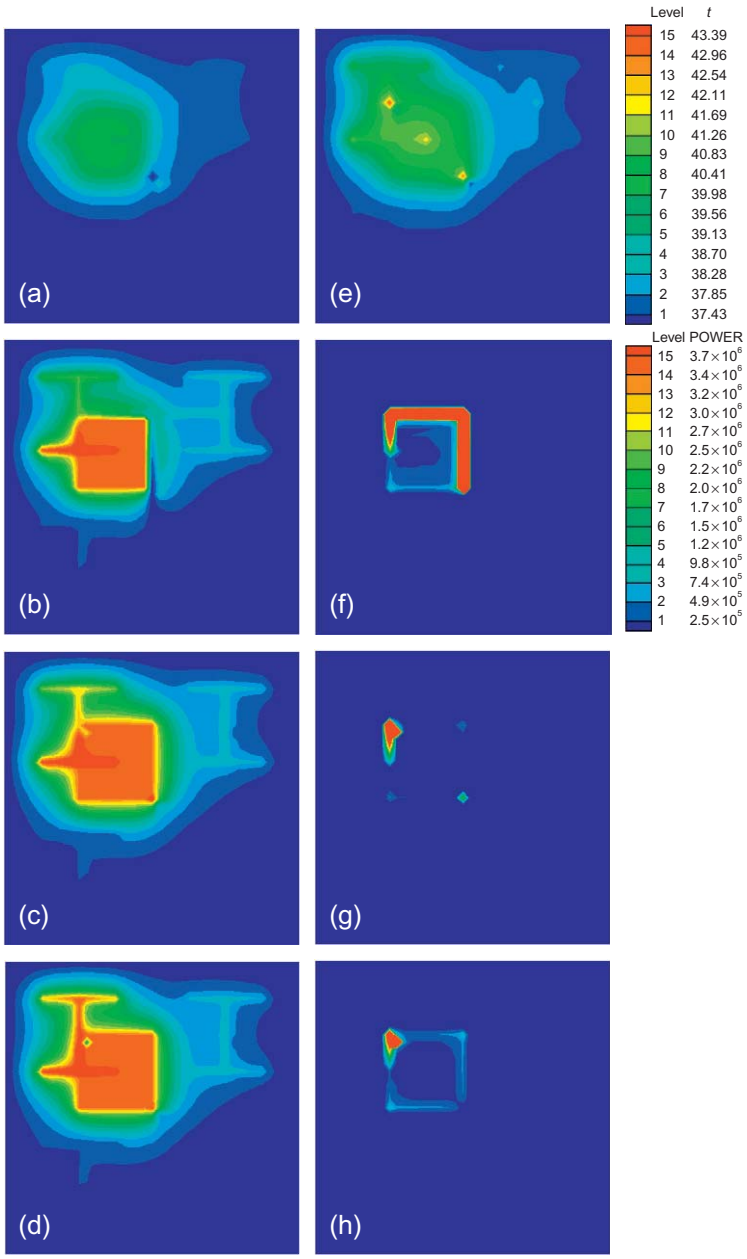

FIGURE 1.18 Temperatures and absorbed power depositions for a blood perfusion rate of 2.0 kg/m^3/s after optimization with fine spatial power deposition. The ideal temperature is set to be 43 °C, and the blood flow velocity is about 1280 mm/s in level 1 vessel. (a-e) are the temperature distributions at $x=38$ mm (4 mm away from the front boundary), $x=42$ mm (the front boundary), $x=52$ mm (middle of the treated region), $x=62$ mm (the back boundary), and $x=66$ mm (4 mm away from the back boundary) planes, respectively, after optimization. (f-h) are the absorbed power depositions at $x=42$, 52, and 62 mm planes, respectively, after optimization (units in figure, t: °C and power: W/m^3).

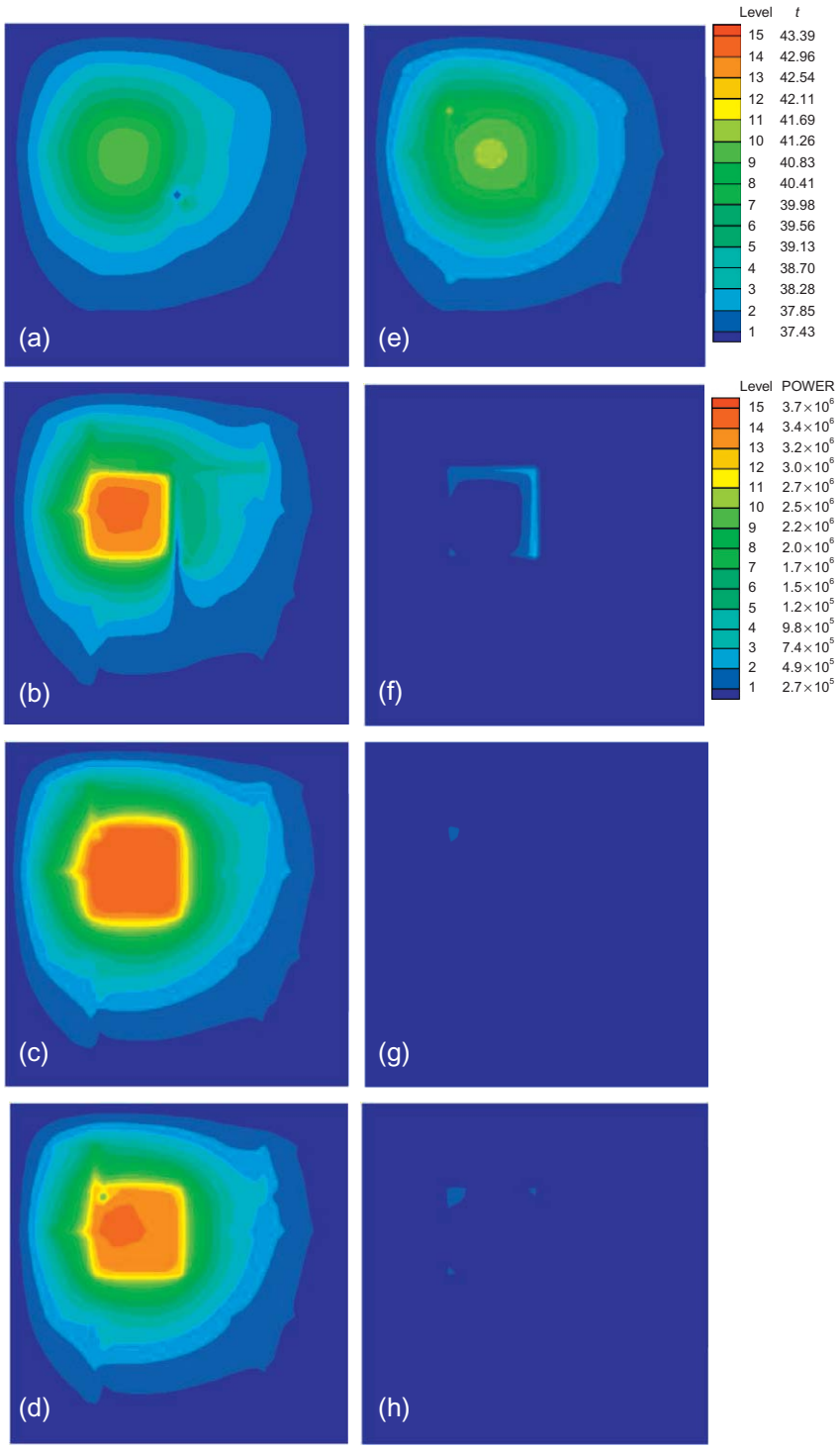

FIGURE 1.19 Temperatures and absorbed power depositions for a blood perfusion rate of 0.123 kg/m^3/s after optimization with fine spatial power deposition. The ideal temperature is set to be 43 °C, and the blood flow velocity is about 80 mm/s in level 1 vessel. (a-e) are the temperature distributions at $x = 38$ mm (4 mm away from the front boundary), $x = 42$ mm (the front boundary), $x = 52$ mm (middle of the treated region), $x = 62$ mm (the back boundary), and $x = 66$ mm (4 mm away from the back boundary) planes, respectively, after optimization. (f-h) are the absorbed power depositions at $x = 42$, 52, and 62 mm planes, respectively, after optimization (units in figure, t: °C and power: W/m^3).

treated region except for some cold spots which are produced by the arteries, the same as in the case of 0.5 $kg/m^3/s$.

Smooth and homogeneous temperatures in treated tumor volume could be achieved easily with less power deposition by using preheating [62]. Furthermore, for a better homogeneous temperature distribution in the treated region, modification of an adaptive optimization scheme is required [63].

1.5.4 Optimization Without Thermally Significant Blood Vessels in the Tissues

The PBHTE is used to investigate temperature and absorbed power deposition in the treated region for the condition without thermally significant blood vessels. A uniform blood perfusion rate of 0.5 $kg/m^3/s$ in the entire tissue was studied using the optimization. Figures 1.20a and e show two unheated parallel temperature distribution planes next to the front boundary plane at 1 and 2 discretization steps. Figures 1.20f-h show the optimized power deposition on the front boundary, the middle, and the back boundary planes, respectively. Most of the power is deposited on the corners and edges of the treated region to compensate for thermal energy loss through conduction due to the strong conductive effects near corners and edges. The deposited power pattern of Figure 1.20h is identical to that shown in Figure 1.20f, and Figure 1.20g (the middle plane of the treated region) shows that there is less power deposited on corners and center area as compared to Figure 1.20f (front boundary plane). It indicates that the thermal diffusion rate is much smaller in the middle region. Figures 1.20b-d show a very uniform therapeutic temperature distribution on the front boundary, the middle, and the back boundary planes, respectively, in the treated region. They can be achieved as there are no thermally significant blood vessels present.

1.5.5 Conclusion

To produce a uniform therapeutic temperature distribution in the desired treated region while minimizing the overheating of the surrounding normal tissue is desirable for hyperthermia treatment. To reach this goal requires a powerful heating system that is able to deposit power in the treated region to raise the temperature of the entire treated region up to the desired value and overcome the loss of energy by blood perfusion, boundary conduction, and blood flow from the vasculature. The temperature results after optimization show the cold spots and/or cold strips along the blood vessels. These temperatures display the tremendous effects of blood vessels on the resulting heating temperature and the limitation of heating systems. A powerful heating system with fine spatial resolution for power deposition has a better ability to deliver suitable power to locally overcome the convective effect caused by the thermally significant vessels. Although a heating system with fine power deposition is a very important factor during treatment, the complexity of existing thermally significant blood vessels plays a crucial role in successful hyperthermia treatments. This complexity is related to mass flow rates, inlet temperatures, and directions of vessels. Therefore, prior to hyperthermia treatments, thermally significant blood vessels should be identified and handled carefully in order to reduce their cooling effects on the treated region, particularly to those vessels flowing into the treated region.

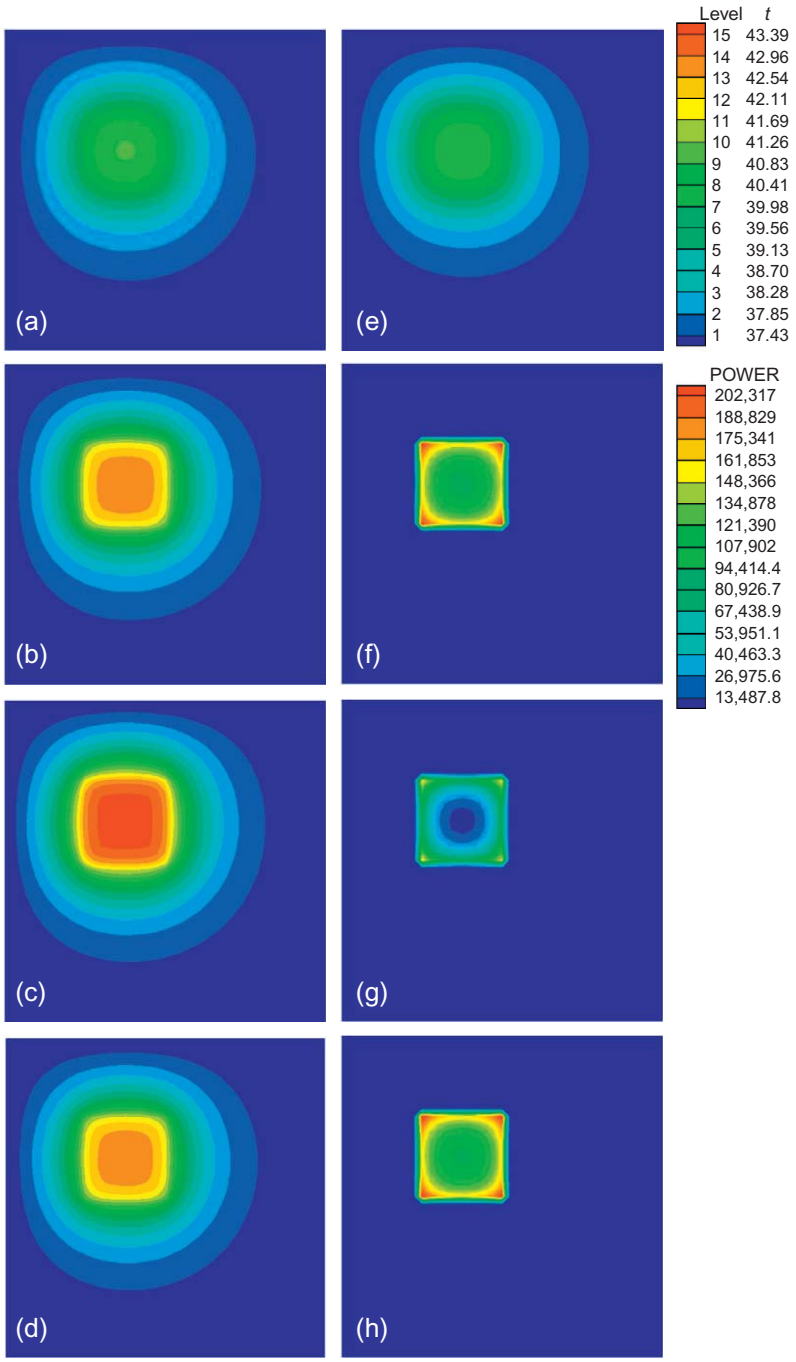

FIGURE 1.20 Temperatures and absorbed power depositions for a blood perfusion rate of 0.5 kg/m^3/s with no vasculature present and after optimization with fine spatial power deposition. The ideal temperature is set to be 43 °C. (a-e) are the temperature distributions at $x=38$ mm (4 mm away from the front boundary), $x=42$ mm (the front boundary), $x=52$ mm (middle of the treated region), $x=62$ mm (the back boundary), and $x=66$ mm (4 mm away from the back boundary) planes, respectively, after optimization. (f-h) are the absorbed power depositions at $x=42$, 52 and 62 mm planes, respectively, after optimization (units in figure, t: °C and power: W/m^3).

References

[1] Pennes HH. Analysis of tissue and arterial blood temperature in the resting human forearm. J Appl Phys 1948;1:93–122.
[2] Roemer RB, Forsyth K, Oleson JR, Clegg ST, Sim DA. The effect of hydralazine dose on blood perfusion changes during hyperthermia. Int J Hyperthermia 1988;4(4):401–15.
[3] Chen MM, Holmes KR. Micro vascular contributions in tissue heat transfer. Ann N Y Acad Sci 1980;335:137–50.
[4] Weinbaum S, Jiji LM. A new simplified bioheat equation for the effect of blood flow on local average tissue temperature. J Biomech Eng 1985;107:131–9.
[5] Wissler EH. Comments on the new bioheat equation proposed by Weinbaum and Jiji. J Biomech Eng 1987;109:131–9.
[6] Wissler EH. Comments on Weinbaum and Jiji discussion of their proposed bioheat equation. J Biomech Eng 1987;109:355–6.
[7] Weinbaum S, Jiji LM, Lemons DE. Theory and experiment for the effect of vascular temperature on surface tissue heat transfer—part 11: model formulation and solution. J Biomech Eng 1984;106:331–41.
[8] Keller KH, Seiler L. An analysis of peripheral heat transfer in man. J Appl Physiol 1971;30:779–86.
[9] Baish JW, Ayyaswamy PS, Foster KU. Small scale temperature fluctuations in perfused tissue during local hyperthermia. J Biomech Eng 1986;108:246–51.
[10] Baish JW, Ayyaswamy PS, Foster KR. Heat transport mechanisms in vascular tissues: a model comparison. J Biomech Eng 1986;108:324–31.
[11] Charny CK, Weinbaum S, Levin UL. An evaluation of the Weinbaum-Jiji bioheat equation for normal and hyperthermic conditions. J Biomech Eng 1990;I(12):80–7.
[12] Charny CK, Levin RL. Bioheat transfer in a branching countercurrent network during hyperthermia. J Biomech Eng 1989;111:263–70.
[13] Nelson DA. Invited editorial on "Pennes' 1948 paper revisited". J Appl Physiol 1998;85:2–3.
[14] Kolios MC, Sherar MD, Hunt JW. Blood flow cooling and ultrasonic lesion formation. Med Phys 1996;23:1287–98.
[15] Kotte A, van Leeuwen G, de Bree J, van der Koijk J, Crezee H, Lagendjik J. A description of discrete vessel segments in thermal modeling of tissues. Phys Med Biol 1996;41:865–84.
[16] Chato JC. Heat transfer to blood vessels. J Biomech Eng 1980;102:110–8.
[17] Lagendijk JJW. The influence of blood flow in large vessels on the temperature distribution in hyperthermia. Phys Med Biol 1982;27:17–23.
[18] Crezee J, Lagendijk JJW. Temperature uniformity during hyperthermia: the impact of large vessels. Phys Med Biol 1992;37:1321–37.
[19] Hariharan P, Myers MR, Banerjee RK. HIFU procedures at moderate intensities-effect of large blood vessels. Phys Med Biol 2007;52:3493–513.
[20] Consiglieri L, dos Santos I, Haemmerich D. Theoretical analysis of the heat convection coefficient in large vessels and the significance for thermal ablative therapies. Phys Med Biol 2003;48:4125–34.
[21] Shrivastava D, Roemer RB. Readdressing the issue of thermally significant blood vessels using a countercurrent vessel network. J Biomech Eng 2006;128:210–6.
[22] He Q, Zhu L, Lemonds DE, Weinbaum S. Experimental measurements of the temperature variation along artery-vein pairs from 200 to 1000 μm diameter in rat hind limb. J Biomech Eng 2002;124:656–61.
[23] Shih TC, Kou HS, Lin WL. Cooling effect of thermally significant blood vessels in perfused tumor tissue during thermal therapy. Int Commun Heat Mass 2006;33:135–41.
[24] Kolios MC, Sherar MD, Hunt JW. Large blood vessel cooling in heated tissues: a numerical study. Phys Med Biol 1995;40:477–94.
[25] Shih TC, Kou HS, Lin WL. The impact of thermally significant blood vessels in perfused tumor tissue on thermal distributions during thermal therapies. Int Commun Heat Mass 2003;30:975–85.
[26] Khanafer K, Bull JL, Pop I, Berguer R. Influence of pulsatile blood flow and heating scheme on the temperature distribution during hyperthermia treatment. Int J Heat Mass Tran 2007;50:4883–90.
[27] Song CW, Lokshina A, Rhee JG, Paten M, Levitt SH. Implication of blood flow in hyperthermia treatments of tumors. IEEE Trans Biomed Eng 1984;31:9–16.
[28] Craciunescu OI, Clegg ST. Pulsatile blood flow effects on temperature distribution and heat transfer in rigid vessels. J Biomech Eng 2001;123:500–5.

[29] Horng TL, Lin WL, Liauh CT, Shih TC. Effects of pulsatile blood flow in large vessels on thermal dose distribution during thermal therapy. Med Phys 2007;34:1312–20.
[30] Fung YC. Biomechanics: motion, flow stress, and growth. New York: Springer-Verlag; 1996.
[31] Nichols WW, O'Rourke MF. McDonald's blood flow in arteries: theoretic, experimental and clinical principles. Philadelphia: Lea & Febiger; 1990.
[32] Huo Y, Kasab GS. Pulsatile blood flow in the entire coronary arterial tree: theory and experiment. Am J Physiol Heart Circ Physiol 2006;291:H1074–87.
[33] Shih T-C, Horng T-L, Huang H-W, Ju K-C, Huang T-C, Chen P-Y, et al. Numerical analysis of coupled effects of pulsatile blood flow and thermal relaxation time during thermal therapy. Int J Heat Mass Tran 2012;55:3763–73.
[34] Sapareto SA, Dewey WC. Thermal dose determination in cancer therapy. Int J Radiat Oncol Biol Phys 1984;10:787–800.
[35] Damianou C, Hynynen K. Focal spacing and near-field heating during pulsed high temperature ultrasound therapy. Ultrasound Med Biol 1993;19:777–87.
[36] Kou HS, Shih TC, Lin WL. Effect of directional blood flow on thermal dose distribution during thermal therapy: an application of Green's function based on the porous model. Phys Med Biol 2003;48:1577–89.
[37] Joseph DD, Preziosi L. Heat waves. Rev Mod Phys 1989;61:41–73.
[38] Özisik MN, Tzou DY. On the wave theory in heat conduction. J Heat Trans-T ASME 1994;116:525–6.
[39] Tzou DY. Marco- to micro-scale heat transfer: the lagging behavior. Washington, DC: Taylor and Francis; 1997.
[40] Kaminski K. Hyperbolic heat conduction equation for materials with a nonhomogeneous inner structure. J Heat Trans-T ASME 1990;112:555–60.
[41] Zhou J, Zhang Y, Chen JK. Non-Fourier heat conduction effect on laser-induced thermal damage in biological tissues. Numer Heat Transfer 2008;54:1–19.
[42] Zhou J, Chen JK, Zhang Y. Dual-phase effects on thermal damage to biological tissues caused by laser irradiation. Comput Biol Med 2009;39:286–93.
[43] Roemer RB, Oleson JR, Cetas TC. Oscillatory temperature response to constant power applied to canine muscle. Am J Physiol 1985;249:R153–8.
[44] Mitra K, Kumar S, Vedavarz A, Moallemin MK. Experimental evidence of hyperbolic heat conduction in processed meat. J Heat Trans-T ASME 1995;117:568–73.
[45] Antaki PJ. New interpretation of non-Fourier heat conduction in processed meat. J Heat Trans-T ASME 2005;127:189–93.
[46] Cattaneo MC. Sur une forme de l'équation de la chaleur éliminant le paradoxe d'une propagation instantaneé. Comptes Rendus de L'Academie des Sciences: Series I-Mathematics 1958;247:431–3.
[47] Vernotte P. Les paradoxes de la théorie continue de l'équation de la chaleur. Comptes Rendus 1958;246:3154–5.
[48] Roetzel W, Putra N, Das SK. Experiment and analysis for non-Fourier conduction in materials with non-homogeneous inner structure. Int J Therm Sci 2003;42:541–52.
[49] Zhang Y. Generalized dual-phase lag bioheat equations based on non-equilibrium heat transfer in living biological tissues. Int J Heat Mass Tran 2009;52:4829–34.
[50] Lagendijk JJ, Hofman P, Schipper J. Perfusion analyses in advanced breast carcinoma during hyperthermia. Int J Hyperthermia 1988;4:479–95.
[51] Huang H, Chan C, Roemer RB. Analytical solutions of Pennes bio-heat transfer equation with a blood vessel. J Biomech Eng 1994;116:208–12.
[52] Crezee J, Lagendijk JJW. Experimental verification of bio-heat transfer theories: measurement of temperature profiles around large artificial vessels in perfused tissue. Phys Med Biol 1990;35:905–23.
[53] Chen ZP, Roemer RB. The effects of large blood vessels on temperature distributions during simulated hyperthermia. J Biomech Eng 1992;114:473–81.
[54] Huang HW, Chen ZP, Roemer RB. A countercurrent vascular network model of heat transfer in tissues. J Biomech Eng 1996;118:120–9.
[55] Mooibroek J, Lagendijk JJ. A fast and simple algorithm for the calculation of convective heat transfer by large vessels in three dimensional inhomogeneous tissues. IEEE Trans Biomed Eng 1991;38:490–501.
[56] Kotte ANTJ, van Leeuwen GMJ, de Bree J, van der Koijk JF, Crezee J, Lagendijk JJW. A description of discrete vessel segments in thermal modelling of tissues. Phys Med Biol 1996;41:865–84.
[57] Kotte AN, van Leeuwen GM, Lagendijk JJ. Modelling the thermal impact of a discrete vessel tree. Phys Med Biol 1999;44:57–74.

[58] Tharp HS, Roemer RB. Optimal power deposition with finite-sized, planar hyperthermia applicator arrays. IEEE Trans Biomed Eng 1992;39(6):569–79.
[59] Lin WL, Liang TC, Yen JY, Liu HL, Chen YY. Optimization of power deposition and a heating strategy for external ultrasound thermal therapy. Med Phys 2001;28(10):2172–81.
[60] Kumaradas JC, Sherar MD. Optimization of a beam shaping bolus for superficial microwave hyperthermia waveguide applicators using a finite element method. Phys Med Biol 2003;48(1):1–18.
[61] Cheng TY, Ju KC, Ho CS, Chen YY, Chang H, Lin WL. Split-focused ultrasound transducer with multidirectional heating for breast tumor thermal surgery. Med Phys 2008;35(4):1387–97.
[62] Huang H-W, Liauh C-T, Horng T-L, Shih T-C, Chiang C-F, Lin W-L. Effective heating for tumors with thermally significant blood vessels during hyperthermia treatment. Appl Therm Eng 2013;50:837–47.
[63] Huang H-W, Liauh C-T, Chou C-Y, Shih T-C, Lin W-L. A fast adaptive power scheme based on temperature distribution and convergence value for optimal hyperthermia treatment. Appl Therm Eng 2012;37:103–11.